Chemical Engineering Journal 544 (2026) 178969

Contents lists available at ScienceDirect

Chemical Engineering Journal

journal homepage: www.elsevier.com/locate/cej

Exhaust gas aftertreatment of dimethyl ether as a challenge for the carbon-neutral fuel in internal combustion engines

Tom Padeken [a,d,e,*], Ariel Augusto Schönberger [a,d,e,*], Nedelina Toshkova [a], Alexander Lampkowski [a], Peter Mauermann [a,d], Daniel Röhrens [b,d,e], Felix Ott [c,d,e], Bastian Lehrheuer [a,e], Stefan Sterlepper [a,d], Ulrich Simon [b,d,e], Regina Palkovits [c,d,e,f], Stefan Pischinger [a,d,e]

[a] TME - Chair of Thermodynamics of Mobile Energy Conversion Systems, RWTH Aachen University, Forckenbeckstrasse 4, 52074, Aachen, Germany
[b] IAC - Chair of Inorganic Chemistry and Electrochemistry, RWTH Aachen University, Landoltweg 1a, 52074, Aachen, Germany
[c] ITMC - Chair of Heterogeneous Catalysis and Technical Chemistry, RWTH Aachen University, Worringerweg 2, 52074, Aachen, Germany
[d] ACA - Center for Automotive Catalytic Systems Aachen, RWTH Aachen University, Schinkelstrasse 8, 52062, Aachen, Germany
[e] FSC - The Fuel Science Center, RWTH Aachen University, Schinkelstrasse 8, 52062, Aachen, Germany
[f] Institute for Sustainable Hydrogen Economy, Forschungszentrum Jülich GmbH, An der Deutschen Welle 7a, 52428, Jülich, Germany

ARTICLE INFO

Keywords:
Oxygenated hydrocarbons
Oxidation catalyst
Selective catalytic reduction
Dimethyl ether
Exhaust gas aftertreatment

ABSTRACT

This study investigates the extent to which existing series exhaust aftertreatment catalysts, such as diesel oxidation catalysts (DOC) and selective catalytic reduction (SCR) catalysts, can be used to reduce emissions of unburned HC slip in the exhaust gas from the use of CO_2-neutral dimethyl ether (DME) in internal combustion engines. It is shown that not all DOCs were able to completely prevent DME slip under the selected, close to realistic conditions such as gaseous hourly space velocity and temperature range. Also, the formation of toxic secondary emissions can be measured, during the light-off experiments. Furthermore, it is shown that depending on the SCR catalyst, the presence of DME at temperatures above $T > 300$ °C can lead to the release of significant amounts of toxic products such as HCN, CH_2O, CH_2O_2 and CO. These could furthermore deactivate the NH_3-SCR catalyst. In addition, the $DeNO_x$-performance is inhibited for the temperature range above $T > 350$ °C, when DME is converted during the SCR. Another novel finding is that the presence of formic acid may lead to a shift in the NO/NO_2 equilibrium and production of NO_2 in the corresponding temperature range.

1. Introduction

Achieving a zero-carbon footprint is essential for sustainability, particularly in light of climate change and the significant anthropogenic impacts. The transportation sector, heavily reliant on fossil fuels, contributes nearly 40% of global CO_2 emissions, underscoring the urgent need for transformation in mobility and energy [1]. While recent efforts have focused on the wider deployment of electric vehicles, questions remain regarding their effectiveness in decarbonization due to concerns about battery life cycle assessments and energy density. A promising alternative lies in the utilization of renewable fuels, particularly dimethyl ether (DME), which offers a sustainable option for diesel substitution in internal combustion engines. DME stands out as a clean synthetic fuel with favorable combustion properties and low emissions [2,3]. Its production from renewable sources not only enhances resource sustainability but also provides an opportunity to reduce reliance on fossil fuels. DME can be derived from various feedstocks through direct or indirect synthesis methods that e.g. convert biomass into synthesis gas before further processing into DME [4,5].

The utilization of renewable resources has the potential to make a substantial contribution to the reduction of greenhouse gas emissions (GHG) as part of the transition to DME. The use of DME in internal combustion engines is twofold: firstly, as a neat fuel and secondly as a DME-diesel fuel blend. This second approach was also investigated in the underlying project. The objective is to preserve as many existing vehicle components as possible and to maintain the DME content at the highest possible level. The objective of this project aims to achieve the most significant possible reduction in GHG emissions in the legacy fleet.

* Corresponding authors at: TME - Chair of Thermodynamics of Mobile Energy Conversion Systems, RWTH Aachen University, Forckenbeckstrasse 4, 52074, Aachen, Germany.
E-mail addresses: Padeken@tme.rwth-aachen.de (T. Padeken), ariel.schoenberger@gmail.com (A.A. Schönberger).

https://doi.org/10.1016/j.cej.2026.178969
Received 17 March 2026; Received in revised form 1 June 2026; Accepted 29 June 2026
Available online 3 July 2026

In this context, it is of particular importance to investigate the response of series production components of the exhaust aftertreatment system to DME-containing exhaust gas. DME is produced from synthesis gas in direct (one-step, Eq. (1)) or indirect (two-step, Eqs. (2) & (3)) way [6].

$$3\ CO_{(g)} + 3\ H_{2\ (g)} \rightarrow CH_3OCH_{3\ (g)} + CO_{2\ (g)} \quad (1)$$

$$CO_{(g)} + 2\ H_{2\ (g)} \rightarrow CH_3OH \quad (2)$$

$$2\ CH_3OH_{(g)} \rightarrow CH_3OCH_{3\ (g)} + H_2O_{(g)} \quad (3)$$

The two-step path goes through the Cu/ZnO-catalyzed synthesis of methanol as intermediate (Eq. (2)) [5] that is further converted to DME over γ-Al_2O_3 or zeolites in dehydration reaction (Eq. (3)) [7] with high selectivity [6]. In the aim of reduced carbon footprint and CO_2 neutrality, a path of DME synthesis from CO_2 is currently under development, which enables the utilization and recycling of CO_2 [6,8,9]. This is achieved by the reverse water gas shift reaction of CO_2-rich synthesis gas (Eq. (4)) or CO_2 hydrogenation to methanol (CH_3OH) (Eq. (5)) [6,9].

$$CO_{2\ (g)} + H_{2\ (g)} \rightarrow CO_{(g)} + H_2O_{(g)} \quad (4)$$

$$CO_{2\ (g)} + 3\ H_{2\ (g)} \rightarrow CH_3OH_{(g)} + H_2O_{(g)} \quad (5)$$

The central part of DME emission characteristics during combustion is its chemical structure. The C—O bond and the absence of a direct C—C bond lead to suppressed soot formation and smokeless combustion [10].

DME has a high cetane number (above 55) which shows a good ability to self-ignite under compression and is related to a better and cleaner combustion [11]. The similarity of DME and diesel fuel cetane numbers is beneficial for the DME applicability to diesel engines [10]. Diesel engines function under lean conditions with a high air-to-fuel ratio, resulting in exhaust gases comprising primarily oxidation products such as CO_2, H_2O (in full oxidation) and NO_x (NO & NO_2), CO, and other hydro carbon (HC) emissions [11]. A conventional diesel exhaust aftertreatment system comprises a diesel oxidation catalyst (DOC), a diesel particulate filter (DPF) and NO_x catalyst (SCR) [11,12]. The supply of a further reducing agent, namely ammonia, is necessary for the reduction of NO_x [13]. The schematic configuration of an exhaust aftertreatment system (EATS) is illustrated in Fig. 1. Notably, an ammonia (NH_3) slip catalyst (ASC) is positioned at the system's terminal point to address ammonia slip, a consequence of the ammonia dosing strategy.

The reduction catalyst converts the raw NO_x emissions into nitrogen and water by the SCR technology. Common reducing agents are hydrocarbons (HC) and NH_3. HC-SCR takes place typically over Ag/Al_2O_3 [14] catalysts and Cu-loaded zeolites, i.e. Cu-ZSM-5 [15–17]. Oxygenated species such as DME have been found to show good NO_x reducing performance [14,17,18]. This technology gives opportunity for direct use of the fuel without the need of an extra reductant. However, it has some drawbacks such as lower stability and higher temperature activity of the catalyst, lower NO_x efficiency so there is a need of process optimization.

NH_3-SCR is the state-of-the-art technology for NO_x control and abatement in diesel vehicles [16,19]. The reducing agent NH_3 is produced in situ from a 32.5% aqueous urea solution via thermal decomposition (Eq. (6)) and hydrolysis (Eq. (7)) [19,20].

$$NH_2CONH_2 \rightarrow HNCO_{(g)} + NH_{3\ (g)} \quad (6)$$

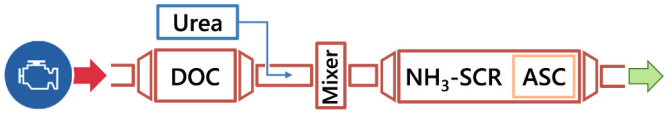

Fig. 1. Scheme of an exhaust aftertreatment system (EATS) as used in modern diesel vehicles.

$$HNCO_{(g)} + H_2O_{(g)} \rightarrow CO_{2\ (g)} + NH_{3\ (g)} \quad (7)$$

SCR can be expressed by three main reactions in dependence to the NO/NO_2 (0, 0.5, > 0.5) ratio [21].

$$4\ NH_3 + 4\ NO + O_2 \rightarrow 4\ N_2 + 6\ H_2O \quad (8)$$

$$2\ NH_3 + NO + NO_2 \rightarrow 2\ N_2 + 3\ H_2O \quad (9)$$

$$8\ NH_3 + 6\ NO_2 \rightarrow 7\ N_2 + 12\ H_2O \quad (10)$$

Eq. (8) shows the standard-SCR reaction, which reduces NO in the presence of oxygen. The slow-SCR (Eq. (10)) reaction occurs, on the other hand, under NO_2 excess. However, as 90% of the released NO_x emission consists of NO, the last process is less probable. The fast-SCR (Eq. (9)) with $NO/NO_2 = 1$ is the optimal process owing to its high reaction kinetics and low temperature conditions [22]. In order to reach it, a DOC oxidizes the excess NO to NO_2 (Eq. (11)).

$$2\ NO + O_2 \rightarrow 2\ NO_2 \quad (11)$$

$$CH_3OCH_3 + 3\ O_2 \rightarrow 2\ CO_2 + 3\ H_2O \quad (12)$$

The primary function of the DOC is the complete oxidation of the raw emissions, including CO and unburned fuel, as described in Eq. (12) [23,24], which is also essential for the SCR system. HC species have a detrimental effect on NH_3-SCR catalyst as they can block the pores by competitive co-adsorption to NH_3 and coke deposition [25–28]. Moreover, they can undergo unselective oxidation and SCR side reactions and promote the formation of further HC intermediate species [26,29].

A wide variety of catalysts show high SCR-activity such as transition metal-based oxides [30,31] and zeolites [32,33]. The small-pore Cu-exchanged zeolites (CHA type) are commercially used for diesel vehicles, owing to their excellent SCR activity over a wide temperature range (T ~ 150–550 °C), [32,34] and a retained hydrothermal stability in presence of chemical poisons (SO_2, HCs) [26,32].

Mechanistic understanding of SCR process over Cu-CHA catalyst is still not complete, despite the detailed experimental and theoretical research [35–37]. The mechanism of the standard SCR is based on the Cu^{II}/Cu^{I} redox cycle [34] and differs in dependence on the temperature [38–40]. Cu^{II} ions act as active site precursors [41,42] for the formation of complexes, solvated by NH_3 und H_2O at low temperature [41,43,44]. Consecutively, reaction with NO leads to the copper ions reduction $Cu^{II} \rightarrow Cu^{I}$ [37,45]. Although the oxidation cycle is even less understood, it is considered to go through a dimeric, oxygenated Cu^{I} structure via oxygen activation, which generates back the Cu^{II} ions [41,45–48].

In recent years it has been established that Cu- and/or Fe-ion exchanged small pore SSZ-13 zeolites, exhibit a remarkable capacity to endure harsh hydrothermal aging conditions at temperatures more than T = 800 °C. This finding signifies that SSZ-13 zeolite can be utilized for extended periods as a component of diesel engine aftertreatment systems, thereby ensuring its long-term functionality [49].

2. Materials and methods

2.1. Sample preparation and characterization methods

A total of six automotive catalysts are being investigated: three selective catalytic reduction (SCR) catalysts and three diesel oxidation catalysts (DOCs). The composition and specific surface area of these catalysts are characterized before their performance in catalytic exhaust gas abatement is evaluated. Exhaust catalyst samples are extracted from a full brick and the channel geometry is documented using a Keyence VHX-500F digital microscope along its entire length. Visible differences in coating technology will be categorized into zones A–C based on their distribution along the length. Sufficient quantities of the catalyst washcoat is removed from the monolithic carrier, ground and analyzed individually for each catalyst with its respective zones. Scanning

electron microscopy (SEM) measurements are conducted using a LEO/ZEISS Supra 35 VP microscope equipped with an INCA x-act detector from Oxford Instruments for energy-dispersive X-ray spectroscopy (EDXRF).

Nitrogen physisorption experiments are performed using an ASAP 2060 instrument (Micromeritics) at T = −196 °C. Prior to each measurement, adsorbates will be removed under a vacuum of p = 2 pa at T = 150 °C for at least 5 h. The specific surface area is determined using the Brunauer-Emmett-Teller (BET) model within the pressure range of 0.13 ≤ p/p_o ≤ 0.29.

Inductively coupled plasma spectroscopy (ICP-OES) analysis was conducted with a Spectroblue ICP-OES device (manufacturer: Spectro) to assess metal content.

To analyze catalytic performance properties at the synthetic gas test bench (SGB), samples with a diameter of 18.9 mm are fixed with a swelling mat inside a titanium canning. Before testing, all samples will undergo hydrothermal de-greening at T = 800 °C for 16 h under 10 vol% water content conditions.

2.2. Synthetic gas test bench setup

The experiments were conducted on the synthesis gas test bench, which has been presented in previous publications and is depicted in Fig. 2 [50–52]. It consists of three main parts: gas dosing, reactor and gas analysis. The construction pipes are made of titanium (grade 2) and heated above T > 120 °C to prevent water condensation and improve heat circulation. All gases are dosed by mass flow controllers (Brooks Instrument LLC, Hatfield, PA, USA) and heat controlled via a self-developed convection heater, controlled by a series of power/temperature controllers, automated by a LabVIEW interface. Liquid water is delivered by a syringe pump (CETONI GmbH, Korbussen, Germany) and a HovaPOR LF-1200 (IAS GmbH, Oberursel, Germany) system, with a following evaporation in a self-developed thermal vaporizer so that it reaches the catalyst in gaseous form. Before entering the reactor, the gases from inert gas and educt gas lines are mixed. The reactor contains the catalyst sample, which consists of a monolith that is insulated with expanding mat and positioned in a titanium canning. A variety of different measuring devices were used for the gas analysis, either downstream of the catalyst or upstream by-passing the catalyst, allowing a crosscheck between the measurement equipment and dosage before and after each experiment: a Multigas 2030 HS FTIR (Fourier Transform Infrared) gas analyzer is utilized to measure CO, CO_2, NO_x, H_2O, DME and other hydrocarbon species. In a serial alignment, a combined system from FEV Europe GmbH is installed, consisting of a condensing unit, followed by a paramagnetic detector (PMD) for O_2 measurements and non-dispersive infrared Sensor (NDIR) for CO_2 and CO measurements. In parallel, a flame ionization detector (FID), to display the total HC, as well as an electron impact ionization mass spectrometry (EIMS) in order to examine potential formed H_2 are installed.

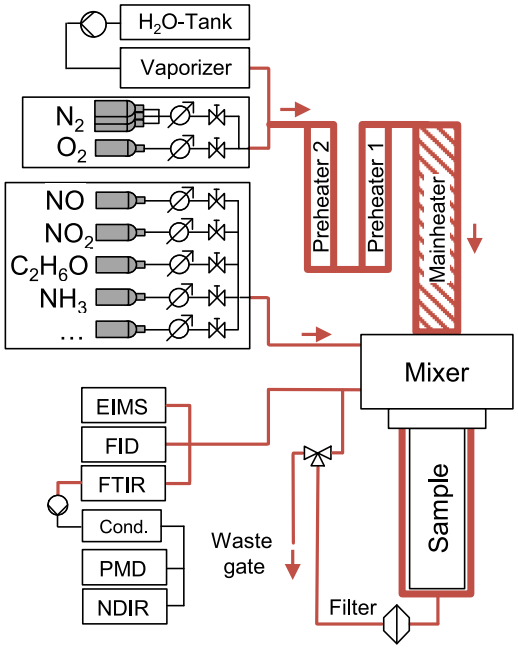

Fig. 2. Schematic representation of the laboratory gas test bench. EIMS: electron-ionization mass spectrometer, FID: flame-ionization detector, FTIR: fourier-transform infrared spectrometer, PMD: paramagnetic detector, NDIR: non-dispersive infrared detector.

2.3. TPR, TPD and light-off procedure

Temperature programmed reduction (TPR) tests (with or without DME) were carried out for each catalyst. The experiments were conducted at a constant gas hourly space velocity of GHSV = 80,000 h^{-1}, which resembles the conditions inside the vehicle under moderate load, in a mixture of c_{H2O} = 10% and N_2 as carrier gas. The NO_2/NO_x varied between 0, 0.5 and 0.75. The experiments started with a pre-conditioning ramp to T = 550 °C to clear the sample from all the adsorbed species. The TPR test included NH_3 adsorption at T = 200 °C (c_{NH3} = 750 ppm), reaction phase at T = 200 °C with all the components (c_{NH3} = 750 ppm, c_{NOx} = 500 ppm, c_{CO2} = 6%, c_{O2} = 10%, c_{DME} = 100 ppm), light-off phase (from T = 200 °C to T = 550 °C), stabilization phase (at T = 550 °C) and light-out phase (from T = 550 °C to T = 200 °C). Consequently, a desorption ramp to T = 550 °C was conducted. To further investigate the catalyst properties, temperature-programmed desorption (TPD) tests were conducted. They included an adsorption phase at T = 150 °C, T = 200 °C, T = 250 °C, T = 350 °C and T = 450 °C (c_{NH3} = 750 ppm, with and without c_{DME} = 500 ppm). Next, the catalyst was flushed with N_2, before being heated at the desorption ramp of $\partial T/\partial t$ = 5 K/min up to T = 550 °C. After a conditioning phase with NO_x (c_{NO} = 250 ppm, c_{NO2} = 250 ppm) at T = 550 °C, the sample was cooled down again. The experiments were carried out at a constant gas hourly space velocity of GHSV = 40,000 h^{-1} in a mixture of 10% H_2O and N_2 as carrier gas. These conditions which resemble a load point of the vehicle under low to moderate load, which can replicate conditions when the urea dosage is initiated. The light-off experiments are part of a larger measurement campaign [53] and in contrast were conducted at a gas hourly space velocity of GHSV = 120,000 h^{-1} to reflect a smaller catalyst carrier volume in an exhaust gas aftertreatment setting. Before and after the main body of the experiment, the catalyst sample was heated, pre- and post-treated at T = 550 °C, with c_{CO} = 700 ppm followed by c_{O2} = 10 vol.-%, both for t = 5 min to free up the sample from adsorbed species and have a controlled oxidized state at the start of the light-off. The main light-off starts at T = 100 °C with a stabilization of the dosed reactants of t = 15 min. The different gas mixtures always contain c_{O2} = 10 vol.-% and c_{H2O} = 8 vol.-%, with c_{DME} = 500 ppm, c_{C3H6} = 250 ppm, c_{CO} = 700 ppm, c_{NO} = 500 ppm and c_{CO2} = 6 vol.-% respectively added for the conducted light-offs, which resembles a real, but simplified raw exhaust mixture. After the stabilization the temperature is ramped to T = 550 °C, with a gradient of $\partial T/\partial t$ = 5 K/min and a consecutive cool down to T = 100 °C, to evaluate the conversion behavior.

3. Results and discussion

3.1. Catalyst characterization

The characterization of the catalysts is summarized in Table 1, which lists the investigated catalysts along with their main properties. This investigation is based on our catalyst matrix, comprising six catalysts, including three DOCs and three SCR catalysts. The nomenclature of all catalysts is set to be DOC 1–3 and SCR 1–3, and is also set from Table 1 onwards. SCR 1 has already been part of a measurement campaign

Table 1
Catalyst characterization overview of SCR 1–3 and DOC 1–3.

Sample	PGM[a] loading/Pt:Pd			Al/Si-ratio/– & [Cu-IEL[b]/%]			BET[c] surface area/(m^2/g)		
Zone	A	B	C	A	B	C	A	B	C
SCR 1 [58]	–	–	–	5.16 [44]	5.16 [44]	–	100	127	–
SCR 2	–	–	–	2.47 [20.01]	2.21 [13.94]	–	270	178	–
SCR 3	–	–	–	2.65 [24.25]	2.32 [18.57]	–	306	218	–
DOC 1	1.12:1	3.63:1	–	0.05 [–]	0.23 [–]	–	160	113	–
DOC 2	1.00:1	1.02:1	0.84:1	0.28 [–]	0.18 [–]	0.17 [–]	63	137	62
DOC 3	0.35:1	0.09:1	0.35:1	0.91 [–]	0.65 [–]	0.67 [–]	155	219	123

[a] PGM – Precious Group Metal.
[b] IEL - Ion Exchange Level, analogue to Gao et al. [57].
[c] BET – Brunauer Emmet Teller.

published by Schönberger et al. [54].

These catalysts are sourced from commercially available series production vehicles, and the washcoat is applied in different zones, A–C. Therefore, separate analysis and characterization must be conducted for each zone. Fig. 3 illustrates the zones for SCR 1 and DOC 1, as determined through optical channel screening. This method allows for the geometric characterization of the zones, serving as a foundation for subsequent chemical analysis.

In this respect, DOC 1 is shown due to the good visible color difference and can be divided into 2 zones (A & B), where the coating of the first and second zone can be clearly differentiated, with the coated length measured from the inlet and outlet being $L_{DOC\ 1,\ A,B} = 41$ mm. The remaining L = 4 mm between zones A and B appears to be uncoated, suggesting that the coating process is by dipping the monolith from the inlet and outlet with the respective catalyst coating. For SCR 1 the channels can visibly be divided into three zones (A, B & C), which can be distinguished by their respective lengths. Zone A has a length of approximately $L_{SCR\ 1,\ A} = 18$ mm, zone B has a length of approximately $L_{SCR\ 1,\ B} = 70$ mm, and zone C has a length of approximately $L_{SCR\ 1,\ C} = 26$ mm. It is evident that the coating is less pronounced in zones A and C. Apart from these observations, no other notable differences in the coating were identified.

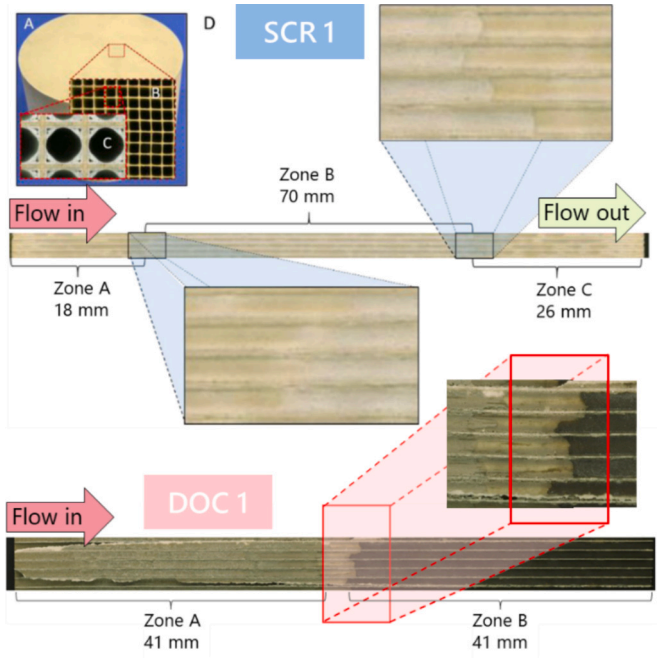

Fig. 3. Optical channel screening of SCR 1 and DOC 1. A, B, C: Channel inlet from the flow direction in increasing magnification. D: Longitudinal channel screening of SCR 1 and DOC 1. The respective channel screenings of SCR 2–3 and DOC 2–3 are to be found in the SI, Fig. S1.

For the remaining four catalysts, the optical channel screenings are displayed in Fig. S1 and the respective lengths of all zones are also displayed in Table S1 for all catalysts.

The SEM images of SCR 1 and DOC 3 zone B are shown in Fig. 4, where the morphology of the obtained catalyst coating can be exhibited, as well as for the additional four catalysts and zones in Figs. S2 to S5. It is to be noted that the preparation of the individual coating samples for chemical analysis is done with a metal spatula and it is always possible that material of the underlying monolith is present and detectable during the SEM, ICP and BET investigations.

As carrier material, cordierite ($Mg_2Al_3[AlSi_5O_{18}]$) is utilized for all six catalysts. The DOCs contain platinum (Pt) and palladium (Pd), with Pt being the more active component for nitrogen oxide (NO) oxidation, while Pd is commonly included due to its lower cost and serving as a long-term stabilizer against thermal aging. Additionally, palladium is often employed in lean combustion settings, as PdO serves as the active state.

Alumina (Al_2O_3) or silica-doped alumina is commonly used as a support material. In DOC 1 zone A, the Pt/Pd ratio is $Pt/Pd_{DOC\ 1,\ A} = 1.12:1$, indicating a bimetallic mix that enhances its thermal stability and which could also promote synergistic effects during catalysis and resistance against HC poisoning [55]. In contrast, DOC 1 zone B features a higher Pt/Pd ratio with $Pt/Pd_{DOC\ 1,\ A} = 3.63:1$, for a suspected optimization of NO oxidation performance. This zone exhibits also increased silicon content, which may suggest the use of silica-doped alumina. This observation could also apply to all three zones in DOC 2. For DOC 3, there is potential for a zeolite-containing coating designed for HC and NO_x storage during cold starts, as these catalysts are referred to as cold start catalysts. A higher silicon content is evident across all three zones. It may be possible that the base layer consists of a zeolite-containing

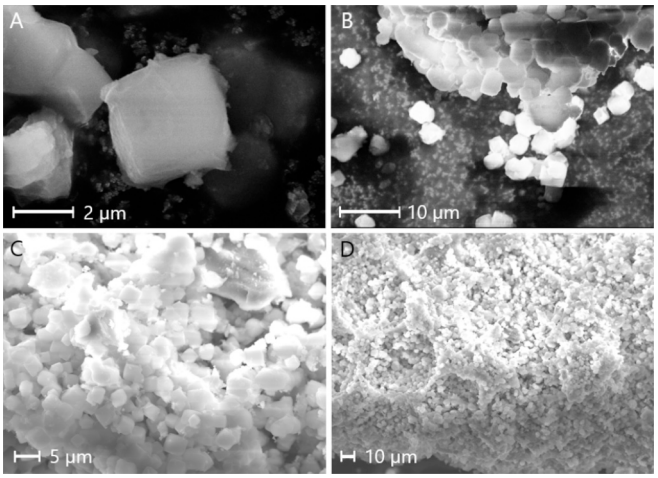

Fig. 4. SEM images of SCR 1 (A, B) and DOC 3 zone B (C, D) in different magnifications. The respective SEM images of SCR 2–3 and DOC 1 and 2 are to be found in the SI Figures (Figs. S2–S5).

washcoat, as described in the patent by Johnson Matthey [56] (WO 2015/150805). In this patent, Pd-exchanged zeolite serves as the base layer for NO_x adsorption, while both the inlet and outlet are additionally coated with either solely platinum or bimetallic Pt/Pd on an alumina support to enhance NO oxidation efficiency. The measured Pt/Pd ratios of the Inlet and Outlet, with $Pt/Pd_{DOC\ 3,\ AB} = 0.35:1$, as well as the middle zone B, with $Pt/Pd_{DOC\ 3,\ B} = 0.09:1$ do indicate the before mentioned coating strategy. The high surface area of $A_{DOC\ 3,\ B} = 219\ m^2/g$, which is on a similar level as the SCR catalysts, also suggests the zeolite containing coating. Another indication of zeolite presence could be determined by the SEM images in the supporting information (SI), where it is noticeable in all three zones, that the appearing structure shows similarities, as presented for the zeolite of SCR 1 in Fig. 4 which has already been characterized in a previous publication [54].

For DOC 2, it is noteworthy that the precious metal group (PGM) loading is significantly higher compared to DOCs 1 and 3. The silicon-to-aluminum ratio ranging from $Al/Si_{DOC\ 2} = 0.170$ to 0.277, with similar wt.-%, suggests that silica-doped alumina support is being utilized. Furthermore, substantial amounts of magnesium are present across all DOCs, implying that cordierite from the monolith might also be retained after sample preparation using a metal spatula. This also could explain the difference in surface area of SCR 1 compared to the other two SCRs, where zone A of SCR 3, with $A_{SCR\ 3,\ A} = 309\ m^2/g$ is three times larger than the surface area of SCR 1. For DOC 1 and 2, the SEM images (Figs. S2 and S3) do not show signs of cubic shaped structures, relating to zeolite containing washcoat, suggesting that no HC or NO_x storage capacity during cold start is targeted, but the high surface area and Pt content indicate an emphasis on NO_x and HC oxidation, with Pd being utilized as a stabilizer for long time performance.

Regarding the SEM images of all SCR catalysts, all samples show zeolite-like morphology with a cubic shape which has been characterized as a chabazite (CHA) structure (ICSD 194282) for SCR 1 via X-ray diffraction, with crystal sizes of approximately 2 µm. SCR 2 and 3 show a smaller crystal size of approx. 1 µm and the ICP results also indicate a Cu-exchanged zeolite, but with lower Ion exchange level, compared to SCR 1. The copper loadings of the zeolites have been calculated according to Eq. (13) below [57].

$$IEL = \frac{n_{Cu}}{n_{Al}} \cdot 2 \cdot 100\% \tag{13}$$

3.2. Oxidation of dimethyl ether on oxidation catalysts

DME is anticipated to emerge as a predominant HC species in the exhaust emissions of DME-operated internal combustion engines (ICEs). Given this projection, the investigated DOCs hold pivotal significance as the initial catalysts in the exhaust aftertreatment system, tasked with the oxidation of HC emissions. Consequently, this chapter focuses on conducting light-off experiments to assess the impact of DME on the performance of these DOC catalysts. The existing literature on DME oxidation offers insights into the behavior and mechanisms of this process.

For reference, in 1996, Solomosy et al. [24] conducted the initial studies on catalytic oxidation. Their study involved various catalysts loaded with rhodium (Rh), palladium (Pd), ruthenium (Ru), platinum (Pt), and iridium (Ir) on an aluminum oxide (Al_2O_3) washcoat. While platinum exhibited the earliest oxidation onset at T = 100 °C, achieving high DME conversion rates of $X_{DME,\ max} = 98–99\%$ at T = 300 °C, the presence of minor quantities of by-products warrants further investigation. However, the low space velocity in these experiments raises concerns regarding the practical applicability of the observed temperature values in real-world exhaust gas aftertreatment systems for combustion engines. Thus, investigations of the three DOCs on the synthetic gas test bench (SGB) were conducted. These light-off experiments mimic applicable lean combustion conditions, including ideal lean combustion conditions and more realistic combustion conditions, to analyze their HC-conversion efficiency and secondary emissions. In Fig. 5, the light-off behavior of DME with a concentration $c_{DME} = 500$ ppm and propene with $c_{C3H6} = 250$ ppm for DOC 1–3 is depicted. Notably, DOC 3 exhibits the fastest light-off for DME at T = 343 °C, along with the highest peak conversion efficiency for both DME and propene of $X_{DME,\ max} = 95\%$ and $X_{C3H6,max} = 99\%$. Conversely, DOC 1 and DOC 2 display the DME light-offs at $T_{50,\ DME} = 355$ °C and $T_{50,\ DME} = 383$ °C, each with a distinct curve trajectory. The higher DME-conversion rate at low temperatures of T < 320 °C and the then decreasing conversion performance of DOC 1 at high temperatures compared to DOC 2 and 3 are attributed to the higher Pt content and the respective PtO formation with rising temperature. While the propene light-off for DOC 1–3 falls within a close range of 162 °C < T < 168 °C, consistent with Hauff et al. [59] and Glover et al. [60]. DOC 1 and DOC 2, unlike DOC 3, achieve a peak conversion efficiency of only $X_{C3H6,\ max} = 96\%$, likely attributable to their relatively high gas hourly space velocity (GHSV).

The analysis of the respective catalysts not only involves assessing DME conversions but also requires a close examination of the resulting by-products. Among these by-products, toxic formaldehyde is noteworthy, as it can be generated during the combustion of oxygenated fuels. Additionally, methanol and formic acid are relevant in this context. Fig. 6 presents the concentrations of formaldehyde detected in two different gas mixtures: one containing only $c_{O2} = 10$ vol% (dashed and light-colored lines) and another that more accurately reflects real exhaust conditions, including $c_{CO} = 700$ ppm, $c_{NO} = 500$ ppm, and $c_{CO2} = 6$ vol% (dark-colored lines). It becomes evident that formaldehyde production is present during the start of the whole time when DME gets converted and additionally rises within the temperature range of T = 300 °C to T = 450 °C for the first gas mixture. DOC 2 achieves the highest concentration peak at $c_{CH2O,DOC2} = 35.5$ ppm at T = 376 °C, while DOCs 1 and 3 show lower peaks at $c_{CH2O,DOC1} = 30$ ppm and $c_{CH2O,DOC3} = 22$ ppm, respectively. This increase in formaldehyde is accompanied by small quantities of formic acid formed within the same temperature range, as depicted in Fig. 6. At T = 375 °C, DOC 2 reaches its maximum concentration of formic acid at $c_{CH2O2,DOC2} = 12.5$ ppm. However, this significant peak is absent in the gas mixture that simulates real engine exhaust for both formaldehyde, formic acid and CO.

When analyzing the overall trends in formaldehyde concentration

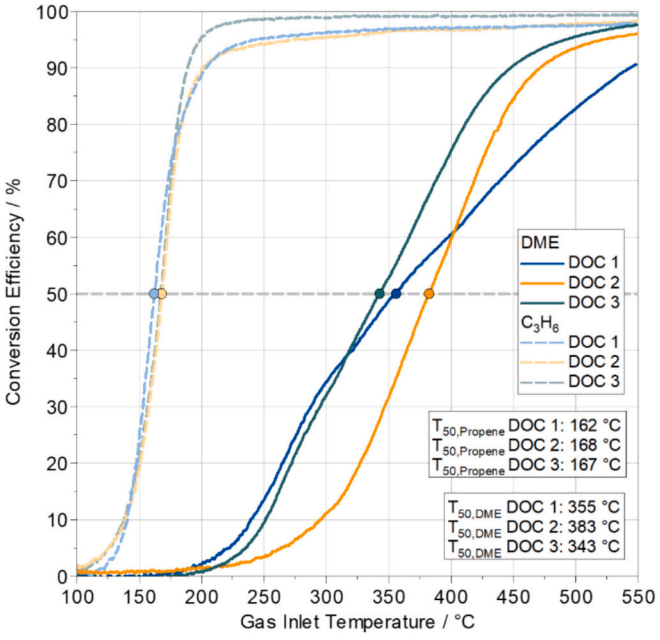

Fig. 5. DME and C_3H_6 conversion efficiency as a function of temperature between 100 °C and 550 °C, $c_{DME} = 500$ ppm, $c_{C3H6} = 250$ ppm, GHSV = 120,000 h^{-1}, $c_{O2} = 10$ vol%, $c_{H2O} = 8$ vol%.

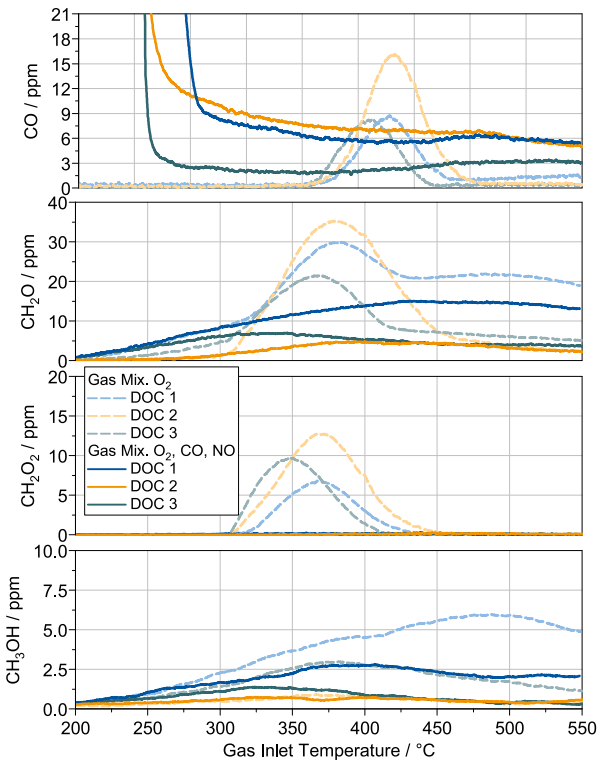

Fig. 6. Formaldehyde, formic acid and methanol concentrations during the DME-light-off (c_{DME} = 500 ppm) experiment with only O_2: c_{O2} = 10 vol% (light, dashed lines) and with O_2: c_{O2} = 10 vol%, CO: c_{CO} = 700 ppm, NO: c_{NO} = 500 ppm and CO_2: c_{CO2} = 6% present (dark, solid lines). For DOC 1 (blue) DOC 2 (orange) DOC 3 (petrol) at GHSV = 120,000 h^{-1}.

across the different catalysts, it becomes apparent that despite its notable peak at T = 376 °C, DOC 2 ultimately emits a lower concentration than DOC 1 offset by Δc_{CH2O} = 10 ppm when considering realistic exhaust conditions. Therefore, the pronounced peak in formaldehyde levels between T = 300 °C and T = 450 °C, which correlates with the increase in formic acid and CO concentration.

Ishikawa et al. [61] outlined a reaction pathway on Pt/γ-Al_2O_3 where DME reacts on the acidic γ-Al_2O_3 support through hydrolysis to generate methanol. This methanol then undergoes oxidation on platinum. As a result, DME conversion increases due to methanol's higher reaction rate. Methanol was also quantified as a product and is displayed in Fig. 6. Furthermore, Peláez et al. [62] describe a process wherein both formaldehyde and methanol are produced concurrently during the selective oxidation of DME over a molybdenum oxide (MoO_x) catalyst. This mechanism is summarized in Eqs. (14), (15) and (16). Initially, two methoxy groups ($CH_3O_{(s)}$) are created through the dissociation of adsorbed DME molecules. These methoxides subsequently react either with oxygen to yield formaldehyde or with hydroxyl groups (OH) to produce methanol.

$$CH_3OCH_{3\,(s)} + O_{(s)} \rightarrow 2\,CH_3O_{(s)} \quad (14)$$

$$CH_3O_{(s)} + O_{(s)} \rightarrow CH_2O_{(s)} + OH_{(s)} \quad (15)$$

$$CH_3O_{(s)} + OH_{(s)} \rightarrow CH_3OH_{(s)} + O_{(s)} \quad (16)$$

Additionally, Liu et al. [63], Cheung et al. [64], and Huang et al. [65] discuss similar oxidation processes involving DME converting into both formaldehyde and methanol over MoO_x catalysts through pathways involving methoxy groups formed upon DME adsorption on oxygen-covered rhodium [66] and Al_2O_3 [67]. The presence of such materials in catalyst samples may contribute to secondary emissions.

Besides the mentioned formaldehyde and formic acid, Fig. 6 shows that in the gas mixture with only c_{O2} = 10 vol%, the peaks are accompanied also by a peak in CO in the same temperature range. The sum of formic acid (CH_2O_2), CO and a multiple of CH_3OH correlates with the formadehyde (CH_2O) concentration over the entire temperature range. Therefore, it appears that CH_2O is formed via two processes: one that also forms CH_3OH, and another that produces CH_2O_2 and CO.

Apart from facilitating the oxidation of hydrocarbons, the DOC also plays a crucial role in converting NO to NO_2, which helps to modify the NO/NO_2 ratio and enhance SCR performance. However, this process can inadvertently lead to the production of the unwanted by-product nitrous oxide (N_2O). It is important to note that a high concentration of platinum (Pt) significantly contributes as a more active catalyst for both the oxidation of NO and the generation of N_2O during this reaction [55,68]. The objective of this study is to investigate how DME influences the efficiency and selectivity of the catalytic reaction. To illustrate this, Fig. 7 presents the concentrations of NO_2 and N_2O obtained from light-off experiments using the gas mixture that closely mimics real exhaust conditions: one without hydrocarbons (depicted by dark, dotted lines), another with additional DME (c_{DME} = 500 ppm) introduced into the same gas mixture (represented by dark, solid lines), and finally one containing propene (c_{C3H6} = 250 ppm) added to the DME gas mixture (light, dashed lines).

In all experiments, distinct variations in the formation of NO_2 were observed among the different catalysts and gas mixtures. The overall trend for NO_2 production from the dosed concentration of c_{NO} = 500 ppm reveals familiar peaks at temperatures of T = 375 °C and T = 425 °C for DOCs 1 and 3, corresponding to maximum concentrations of $c_{NO2,max}$ = 178 ppm and $c_{NO2,max}$ = 166 ppm, respectively. In contrast, DOC 2 displayed a lower total NO_2 output with two separate peaks occurring at lower and higher temperatures, specifically at T = 217 °C and T = 418 °C. These findings do not align well with the measured platinum content in the catalysts, as platinum is generally considered to be the primary active agent for NO oxidation [69]. While DOCs 1 and 3 exhibited similar behaviors despite having significantly different Pt/Pd ratios, DOC 2 showed a divergent oxidation behavior compared to DOC

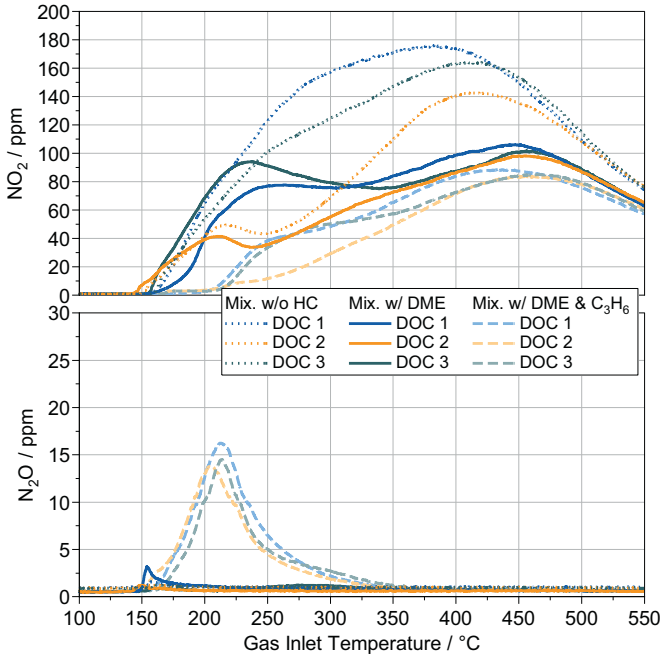

Fig. 7. NO_2 and N_2O concentration for DOC 1 (blue) DOC 2 (orange) DOC 3 (petrol) during the light-off with O_2: c_{O2} = 10%, CO: c_{CO} = 700 ppm, NO: c_{NO} = 500 ppm and CO_2: c_{CO2} = 6% (dark, dotted lines), with DME: c_{DME} = 500 ppm added to the same Mix (dark, solid lines) and with Propene: c_{C3H6} = 250 ppm added to the DME Mix (light, dashed lines).

1 while also maintaining a Pt/Pd ratio exceeding one. Such variations are often linked to the respective roles of Pt or Pd during the reaction; when palladium primarily influences the process, low-temperature NO oxidation can be considerably restricted [60]. Additionally, factors such as surface area, platinum group metals (PGM) dispersion, and other catalytic active sites, such as those present in zeolites play critical roles in shaping reaction outcomes.

When c_{DME} = 500 ppm is added to the mixture, all DOCs demonstrated reduced NO_2 formation in the intermediate temperature range starting from T > 200 °C. This led to a local minimum followed by a decrease in maximum production levels. The initial peak of NO_2 was located between T = 205 °C for DOC 2 and T = 260 °C for DOC 1. A second peak emerged within a narrower temperature range from T = 436 °C for DOC 1 to T = 450 °C for DOC 2. Remarkably, maximum NO_2 generation during the first peak occurred with DOC 3 at c_{NO2} = 93 ppm, while DOC 1 produced the highest amount during the second peak at c_{NO2} = 107 ppm. The reduction in NO_2 formation was particularly noted within the intermediate temperature region where DME begins its conversion on their respective DOCs.

The introduction of propene into this gas mixture completely inhibited NO_2 production up to T = 205 °C; at this temperature point, N_2O was generated with a maximum concentration of $c_{N2O,max}$ = 17 ppm. This well-documented phenomenon [60,70] corresponds with the initiation of propene light-off illustrated in Fig. S6, where propylene inhibits sufficient oxygen coverage required for effective NO oxidation while acting as a reductant.

In summary, concerning secondary emissions of N_2O, it can be concluded that DME does not have a significant effect on its formation. In contrast to DME, existing literature and our tests suggest that propene has a well-established influence on secondary emission generation and notably affects deactivation processes related to NO oxidation [71]. Consequently, DME slip within exhaust gases is considered more favorable.

3.3. Influence of dimethyl ether on SCR catalyst

3.3.1. Temperature programmed desorption (NH_3-TPD)

To investigate further interactions of DME in the subsequent exhaust gas aftertreatment system, namely the NH_3-SCR, NH_3-TPD measurements in the presence and absence of DME were conducted. These investigations are very effective to determine, whether the hydrocarbons will affect the later discussed SCR mechanism by competitive adsorption and direct adsorption with NH_3. In order to start the SCR reaction, it is generally agreed in the literature that ammonia must first be adsorbed on the catalyst's free active sites [27]. From this, a competitive or direct adsorption with DME can be harmful to the desired NO_x abatement via NH_3-SCR. Fig. 8 displays the desorbed amount of NH_3 during the TPD experiments with and without DME, plotted over the gas inlet temperature. The specific released amount NH_3 jumps directly to an elevated value due to the integration of the desorbed NH_3 during the 5 min N_2 flushing. The results in Fig. 8 show that at low temperatures (T = 150 °C, T = 200 °C, T = 250 °C) the same amount of NH_3 is stored regardless of DMEs presence. For the adsorption temperature of T = 250 °C, the maximum difference reaches only $\Delta m_{NH3stored}$ = 1.14%. During these temperatures the DME is slipped through the catalyst and no decomposition and reaction species are detected during the adsorption and desorption phase. Due to their small pores, Cu-CHA shows only a minor influence on NH_3 adsorption for non-oxygenated HC in the literature. Li et al. [72] suggest, that even with NH_3 and C_3H_6 in the feed gas, a strong NH_3 adsorption on zeolite Fe-ZSM-5 is present. Also cohering to our data and similar to Luo et al. [73], where adsorption experiments show that propene did not influence NH_3 adsorption on a Cu/beta zeolite.

In contrast, the presence of another species could lead to competition for active centers with NH_3 [27,74]. As Heo et al. [75] anticipate that C_3H_6 indeed can compete with NH_3 on either a Fe- and Cu-ZSM-5 zeolite, where the adsorbed NH_3 amounts to only 58% for the Cu-, and 60% for the Fe-zeolite at room temperature. Thus, this is retarding a latter examined SCR.

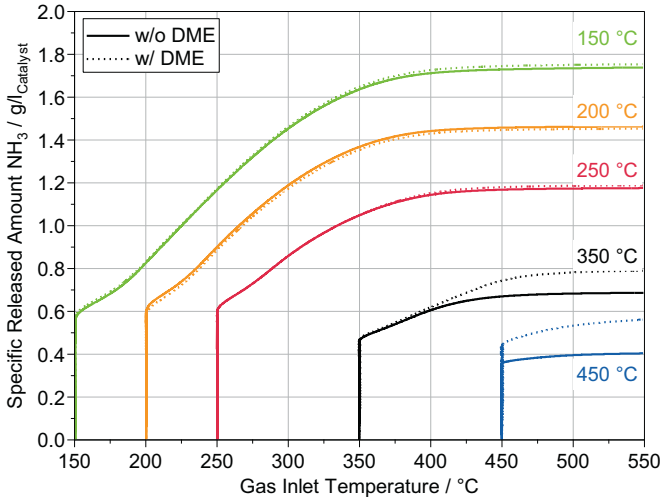

Fig. 8. NH_3-TPD with c_{NH3} = 750 ppm at temperatures of T = 150, 200; 250, 350, 450 °C. Dotted lines with DME and solid lines without c_{DME} = 500 ppm during adsorption.

With regard to the before mentioned literature and the minor competition of DME and NH_3, it can be anticipated, that the adsorption of DME will have no influence on the SCR.

For the temperatures T = 350 °C and T = 450 °C the desorbed amount of NH_3 rises for the parallel dosing of DME. For T = 350 °C the difference reaches $\Delta m_{NH3stored}$ = 15.25% and $\Delta m_{NH3stored}$ = 41.04% at T = 450 °C respectively. During these two experiments, DME either reacts or gets decomposed during the NH_3 adsorption phase. The DME conversion mainly results in CH_3OH, CH_2O, H_2, CO, CO_2 and HCN. This with a toned dependence on the NH_3 surface coverage during the start of the adsorption. Pre-adsorbed oxygen on the surface leads to the initially high CO_2 formation rate, with an initial peak of c_{CO2} = 250 ppm, for the experiment at the temperature of T = 450 °C. At the end of the adsorption phase, the CO_2 concentration settles at c_{CO2} = 32 ppm, aside a great quantity of hydrogen, with c_{H2} = 537 ppm. The main quantity of the produced hydrogen can be associated to the decomposition of DME, but also the water-gas shift reaction, according to Eq. (17), contributes to the H_2-slip.

$$CO + H_2O \rightleftharpoons CO_2 + H_2 \quad (17)$$

The HCN production seems to be dependent to the NH_3 surface coverage, since HCN peaks T_{start_dosing} = 55 s after the dosing start, with c_{HCN} = 60 ppm, which represents a state with approx. 50% of the NH_3-storage capacity of the catalyst at T = 450 °C. Schönberger et al. [54] postulates the formation and followed decomposition of hexamethylenetetramine (HMT or $(CH_2)_6N_4$) from the reaction of ammonia and formaldehyde (Eq. (18)) on hydroxyl groups coordinated to copper centers of the same Cu-SSZ-13 catalyst.

$$4\,NH_3 + CH_2O \rightarrow (CH_2)_6N_4 + 6\,H_2O \quad (18)$$

This statement could also hold for the experiment at T = 350 °C, where approx. c_{DME} = 25 ppm get converted and trace amounts of CH_2O (c_{CH2O} = 2.5 ppm) are produced and slipped, besides the production of c_{MeOH} = 40 ppm, during the NH_3 adsorption phase. Thus, allowing the reaction according to Eq. (18). Since close to no HCN is detected, we conclude the formation of HMT without its immediate decomposition. The decomposition could be associated to the desorbed species during the consecutive temperature ramp, where additional to the expected NH_3 desorption, CH_2O and CH_3OH are desorbed which is an indicator, that DME is decomposed and CH_2O is formed on the catalyst. Thus, strengthening our postulated theory of HMT formation according to Eq.

(18). H_2 and CO are also emitted during the peak at T = 420 °C, as well as NH_3, which suggests HMT decomposition according to Schönberger et al. [54] and the similarity of an enlarged NH_3 storage capacity is also displayed due to an additional NH_3 peak at T = 435 °C.

The potential reaction between NH_3 and NH_3 is only detectable at temperatures, when DME is decomposed and CH_2O could be adsorbed onto active Cu-sites. Thus, only for the TPD-temperatures of T > 350 °C reactions are noticeable.

3.3.2. Oxidation of dimethyl ether on SCR catalyst

Under SCR-relevant conditions, which are mainly characterized by an excess of oxygen in the exhaust gas (c_{O2} = 10 vol%), various oxidation reactions with DME take place, on the three different series catalysts. The experimental conditions are mimicking an exemplary exhaust gas with an excess of O_2, CO_2 (c_{CO2} = 6 vol%) H_2O (c_{H2O} = 8 vol%), as well as NO_x and potential hydrocarbons (here DME) for the main TPR-temperature ramp. The gaseous hourly space velocity of GHSV = 80,000 h^{-1} also corresponds to the values expected in a passenger car exhaust aftertreatment system at medium loads. This experimental phase begins with a pre-conditioned catalyst at T = 550 °C and NH_3 being completely pre-adsorbed at T = 200 °C. From this, the following products can be detected as products of an uncomplete oxidation during the NH_3-SCR, by means of the measurement methods used: CH_3OH, CH_2O, H_2, CO and HCN. The formation of CO_2 and H_2O is hard to quantify due to their dosage in the percentage range. These two products of complete oxidation are considered to be in a high temperature range. In Fig. 9 a similar behavior of the CH_3OH and CH_2O is displayed exemplary for all three catalysts. Here, peaks at different temperatures show a uncomplete oxidation of DME, suggesting different reaction mechanisms, discussed subsequently. The magnitude of the CH_3OH-peak varies from c_{CH3OH} = 13.2 ppm for SCR 2 up to c_{CH3OH} = 25.5 ppm for SCR 3 in the temperature region of 395 °C < T < 408 °C with SCR 1 enclosed by the other two. The same order is detected for the peak in the CH_2O concentration, with a factor of 3.2, between SCR 2 and SCR 3. From an emission performance stand point, SCR 2 would be favorable for an automotive setting.

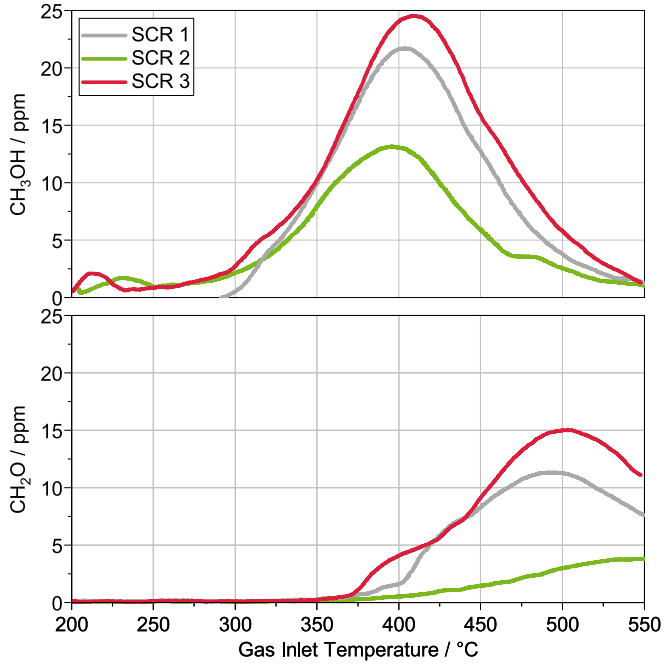

Fig. 9. Detected methanol and formaldehyde concentration during NH_3-SCR in the temperature range between T = 200 °C and T = 550 °C, c_{NH3} = 750 ppm and α = 1.5, at NO_2/NO_x = 0.5. Additional DME concentration during SCR of c_{DME} = 100 ppm, for GHSV = 80,000 h^{-1}.

With respect to differing NO_2 contents in the exhaust gas mix, as expected with increasing temperature, the reactivity of DME increases, which can be observed from the conversion curves in Fig. 10. Between T = 240–260 °C the DME oxidization starts, while from T = 300 °C the conversion increases in significant amounts at higher rates. All samples reach a maximum value in the range of 80%. The light-off temperature is the temperature at which a substance is converted to 50% and thus a measure of the catalyst activity.

It is apparent that SCR 1 achieves a 50% conversion for the NO_2/NO_x ratio smaller 50%, at a higher temperature of T = 427 °C compared to the other catalysts. The NO_2 content seems to have the effect, that in the experiment with excess NO_2, a direct oxidation of DME and NO_2 occurs and the light-off shifts to a lower temperature of T = 417 °C and T = 405 °C respectively. This can be attributed to the oxidative properties of NO_2. Only a little effect on the light-off temperature can be measured for SCR 2, which is at a temperature of T = 412 °C for all NO_2 contents. A bigger effect on the other hand can be observed at 270 °C < T < 320 °C, where a peak for NO_2/NO_x = 0.75 is formed. This is at the temperature area, where the previously formed ammonium nitrate is decomposed and a N_2O-peak is formed, as a byproduct and displayed in the supplemental information (Fig. S7).

SCR 3 shows no direct correlation between the light-off temperature and the NO_2 content. With a NO_2/NO_x ratio of 0.75, the 50% conversion is reached at T = 408 °C as the lowest temperature.

3.3.3. Influence of dimethyl ether on SCR reactions

The experiments have shown that DME dosage during NH_3-SCR produces methanol, carbon monoxide, formaldehyde, formic acid and hydrogen cyanide as products. SCR 1 forms more CH_3OH and CH_2O in comparison to SCR 2 which favors the production of HCN. SCR 3 gives the highest peak concentration of methanol and hydrogen cyanide (Figs. S7 and S8).

Furthermore, in the aim of inspecting the influence of DME concentration, further experiments have been conducted on SCR 1 with c_{DME} = 100 ppm/250 ppm/500 ppm. A rise in the DME concentration leads to higher concentrations of the previously mentioned products. This proves that under SCR conditions DME forms the same products, regardless of its concentration. Nevertheless, slight differences are

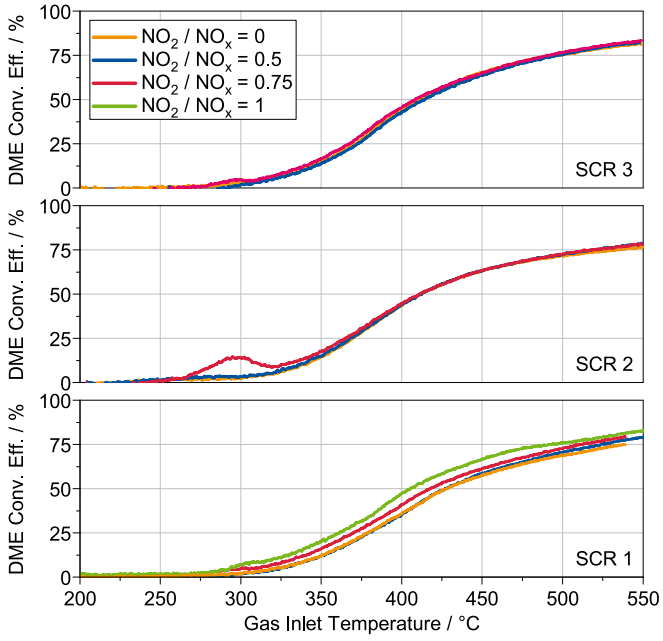

Fig. 10. DME conversion rate as a function of temperature between T = 200 °C and T = 550 °C for all 3 SCR catalysts at varying NO_2/NO_x-ratios of NO_2/NO_x = 0/0.5/0.75/1.

observable such as improvement of the light-off temperature (Fig. 11) and earlier detection of some products. In the following section the formation of HCN, CH_2O, CH_2O_2, CO and the detected effect on the $DeNO_x$ performance are discussed.

The formation of HCN is supposedly related to NO [76]. The mechanism starts with the decomposition of DME into two methyl radicals (Eq. (19)) which then react with NO radical to produce HCN (Eq. (20)) [76,77].

$$CH_3OCH_2\cdot + O_2 \rightarrow 2\cdot CH_3 + H_2CO \quad (19)$$

$$2CH_3 + \cdot NO \rightarrow HCN + H_2O \quad (20)$$

Consequently, HCN can get hydrolyzed to NH_3 and CO (Eq. (21)) [78]. This can also explain the slight stagnation of NH_3 concentration decrease between T = 410 °C and T = 445 °C, which is more recognizable with higher DME concentration (Fig. 12).

$$HCN + H_2O \rightarrow NH_3 + CO \quad (21)$$

At higher temperatures, DME seems to improve the NH_3 conversion. The higher DME dosing concentration, the less NH_3 slip is observed at T = 550 °C. Due to the lack of detected HCN at this temperature as well as decreased NO_x efficiency, it could be concluded that NH_3 side reactions are predominantly favored.

The mechanism of DME oxidation has been extensively studied [76,79–81]. Tamm et al. have proposed a mechanism, based on studying DME reactivity in the gas phase and as SCR agent [80]. Formaldehyde is a common product which is here observed at around T = 360 °C. The concentration increases at around T = 400 °C correlates with the oxidation of methanol (Eq. (22)) [82].

$$2CH_3OH + O_2 \rightarrow 2\ CH_2O + 2\ H_2O \quad (22)$$

The mechanisms according to Tam et al. starts with reaction between DME and hydroxyl radical that delivers a methoxymethyl radical (Eq. (23)) [81].

$$CH_3OCH_3 + \cdot OH \rightarrow CH_3OCH_2\cdot + H_2O \quad (23)$$

The methoxymethyl radical reacts further with oxygen to the reactive peroxy radical (Eq. (24)) which gets isomerized easily (Eq. (25)) [81].

$$CH_3OCH_2\cdot + O_2 \rightarrow 2\ CH_3OCH_2OO\cdot \quad (24)$$

$$CH_3OCH_2OO\cdot \rightarrow CH_2OCH_2OOH\cdot \quad (25)$$

$CH_2OCH_2OOH\cdot$ produces formaldehyde via thermal decomposition as chain propagation (Eq. (26)) or via chain branching reaction with oxygen (Eq. (27)).

$$CH_2OCH_2OOH\cdot \rightarrow 2\ CH_2O + OH\cdot \quad (26)$$

$$CH_2OCH_2OOH\cdot + O_2 \rightarrow CH_2O + 2\ OH\cdot + HCOO\cdot \quad (27)$$

Another important species of DME chemistry is formic acid. In the experiments with dosing of c_{DME} = 100 ppm, only around 1 ppm CH_2O_2 is produced, which lies under the detection limit of the gas analyzing devices. However, with increasing DME concentration (c_{DME} = 250 ppm/500 ppm), CH_2O_2 is detected at higher amounts (c_{CH2O2} = 10 ppm/15 ppm) which proves its role as intermediate and product (Fig. 13).

Tamm et al. suggest that its formation is related to formaldehyde (Eqs. (28) & (29)).

$$CH_2O + OH\cdot \rightarrow CH_2O_2 + H\cdot \quad (28)$$

$$CH_2O + HCOO\cdot \rightarrow CH_2O_2 + CHO\cdot \quad (29)$$

We have observed that in the case of the experiment with c_{DME} = 500 ppm, a local maximum of the formic acid concentration at T = 520 °C is present (Fig. 13). The peak corresponds with the decrease in formaldehyde concentration. Alternatively, DME can produce directly formic acid, together with a methoxymethyl radical (Eq. (30)) [79].

$$CH_3OCH_3 + HCOO\cdot \rightarrow CH_2O_2 + CH_3OCH_2\cdot \quad (30)$$

With regard to additional data, displayed in Figs. S9 and S10, where similar tests are conducted with a catalytically active particulate filter from series production vehicles, the improvement in the DME-light-off temperature for an increasing DME content, as previously seen in Fig. 11, can be associated to the direct reaction of DME to formic acid, according to Eq. (30). During these tests with c_{DME} = 500 ppm, formic acid was formed exclusively in the temperature range of 328 °C < T < 428 °C. Simultaneously, formaldehyde and carbon monoxide are

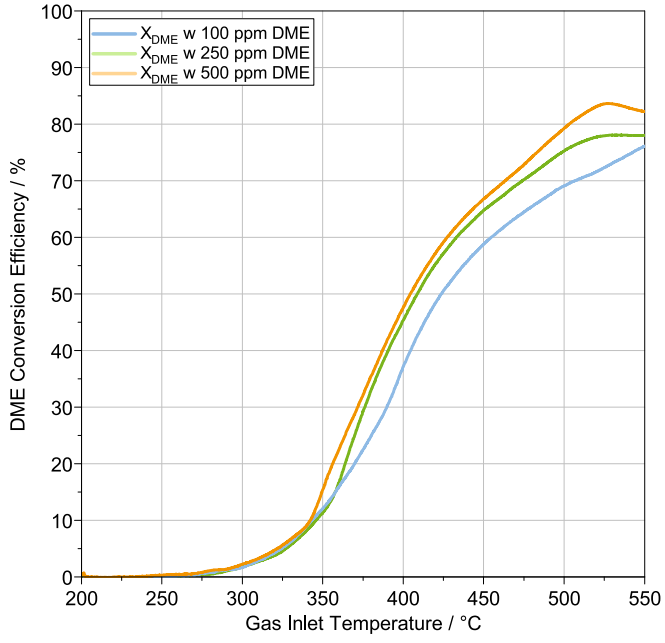

Fig. 11. The conversion of DME and the light-off-temperature between T = 200 °C and T = 550 °C in regard to the DME dosing concentration at a NO_2/NO_x ratio of 0.5 during NH_3-TPR.

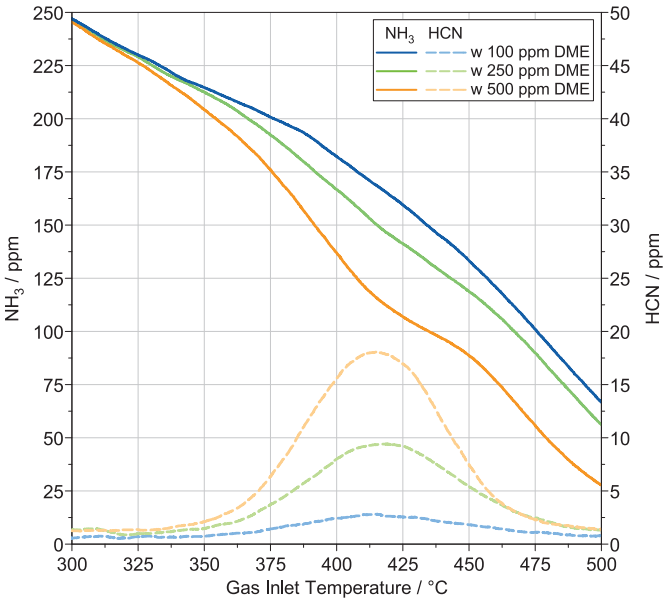

Fig. 12. The concentration of NH_3 (dark, solid lines) and HCN (light, dashed lines) between T = 320 °C and T = 500 °C at NO_2/NO_x ratio of 0.5 with DME dosing concentration of c_{DME} = 100 ppm (orange), c_{DME} = 250 ppm (green), c_{DME} = 500 ppm (cyan), during the NH_3-TPR, under fast SCR conditions.

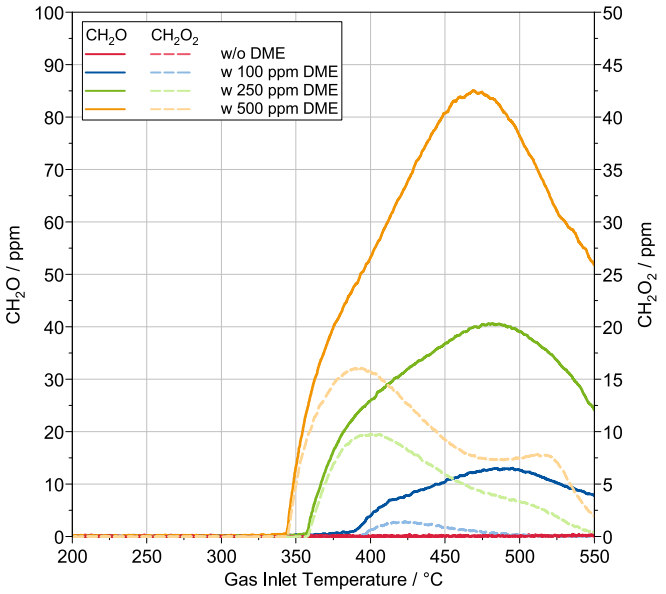

Fig. 13. The concentration of formaldehyde (dark, solid lines) and formic acid (light, dashed lines) in the case of c_{DME} = 100 ppm (blue), c_{DME} = 250 ppm (green), c_{DME} = 500 ppm (orange) and c_{DME} = 0 ppm (red) during the NH_3-TPR, under fast SCR conditions.

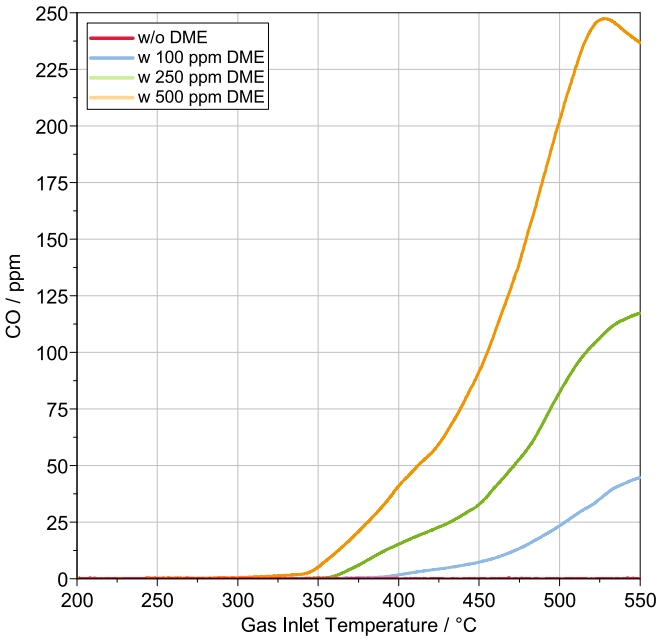

Fig. 14. The concentration of carbon monoxide during the NH_3-TPR in the case of c_{DME} = 100 ppm (light blue), c_{DME} = 250 ppm (green) and c_{DME} = 500 ppm (orange) for fast SCR conditions.

detected. During the same experiment with c_{DME} = 100 ppm, no formic acid can be measured, as well as no characteristic improvement in the DME-conversion for this temperature range. The difference in DME-conversion between these two measurements (with c_{DME} = 100 ppm and c_{DME} = 500 ppm) correlates exactly with the difference in formic acid produced, thus confirming the direct reaction of DME to formic acid, as well as its further reaction to CO, discussed later.

The third formation way starts with the $OCH_2OCHO\cdot$ radical, which can be formed from the product of Eq. (26). This product firstly undergoes isomerization (Eq. (31)) [79]. This isomer then decomposes thermally (Eq. (32)) to produce a species that delivers formic acid via hydrogen radical elimination (Eq. (33)) [79].

$$OCH_2OCHO\cdot \rightarrow HOCH_2OCO\cdot \quad (31)$$

$$HOCH_2OCO\cdot \rightarrow HOCH_2O\cdot + CO \quad (32)$$

$$HOCH_2O\cdot \rightarrow CH_2O_2 + H\cdot \quad (33)$$

The decomposition of formic acid is observed under T = 400 °C in the presence of higher DME concentration (Fig. 13). It can occur by the following reactions (Eqs. (34) to (36)) [79]. CO can be a product of the decomposition of all discussed hydrocarbons and HCN (Eq. (21)). This is the reason why it can be detected at very high concentrations (up to c_{CO} = 250 ppm) (Fig. 14).

$$CH_2O_2 + OH\cdot \rightarrow CO_2 + H_2O + H \quad (34)$$

$$CH_2O_2 + H_2O \rightarrow CO + H_2O_2 + OH \quad (35)$$

$$CH_2O_2 + O\cdot \rightarrow CO + 2\,OH\cdot \quad (36)$$

Its formation is favored at lower temperatures (above T > 320 °C) with increasing DME quantity. (Fig. 14) The formic acid decomposition pathways to CO are shown by Eqs. (34) to (36). A significant part of CO can be formed though methanol (Eq. (37)) and formaldehyde (Eq. (38)) [82].

$$CH_3OH \rightarrow CO + 2H_2 \quad (37)$$

$$CH_2O \rightarrow CO + H_2 \quad (38)$$

For c_{DME} = 500 ppm, the formation of CO reaches a maximum as high as c_{CO} = 248 ppm at T = 525 °C, in contrast to the other experiments (Fig. 14). We assume that the formation and further reaction of CH_2O/CH_2O_2 takes a big part in the CO-peak, because its shape correlates to the corresponding formation. Also, for the experiments with the catalytically active particulate filter, a temperature range (328 °C < T < 428 °C) can be worked out, where the formed CO can be directly associated to the formation reaction of formic acid (Figs. S9 and S10).

Overall, DME has a negative influence on the NO_x conversion efficiency and thus the $DeNO_x$ potential for the use in an automotive setting. The NO_x conversion efficiency is calculated as follows:

$$\eta_{NO_x} = \frac{c_{Dosed,NO} + c_{Dosed,NO_2} - c_{NO_x}}{c_{Dosed,NO} + c_{Dosed,NO_2}} * 100\% \quad (39)$$

In Fig. 15, the NO_x conversion efficiency begins to deviate from the curve with 0% DME, when the DME starts to convert. The magnitude of the difference is dependent on the DME concentration and reaches its maximum of $\Delta\eta_{NOx}$ = 15% at T = 550 °C for c_{DME} = 500 ppm.

The detailed experiments with variation of the DME concentration, shown in Fig. 15 give also insights about the NO_2/NO_x equilibrium. It is visible that NO_2 gets produced at elevated temperatures with higher DME concentrations. This stands in contrast with the usual measured concentrations of NO and NO_2 for the SCR experiment with no DME, which means that the side reaction products may induce a shift in the NO_2/NO_x equilibrium. This is particularly true for the temperatures from T = 392 °C (c_{DME} = 100 ppm), T = 360 °C (c_{DME} = 250 ppm) and T = 343 °C (c_{DME} = 500 ppm) onwards where NO_2 formation is favored, as shown in Fig. 15. This gets partly supported by the results from the investigation on the previously mentioned catalytically active particulate filter, displayed in the supplementary information (Figs. S9 and S10). The production of NO_2 could be linked to the temperature range, where CH_2O_2 is produced in excess at 328 °C < T < 428 °C, for an experiment with c_{DME} = 500 ppm, during the NH_3-SCR experiment.

For SCR 1, in combination with additional experiments, where no NO_2 is dosed during SCR, it can be confirmed that NO_2 is formed and not slipped during the $DeNO_x$ reaction (Figs. S11 and S12). Thus, the data indicates that the presence of CH_2O_2 enhances the formation towards NO_2.

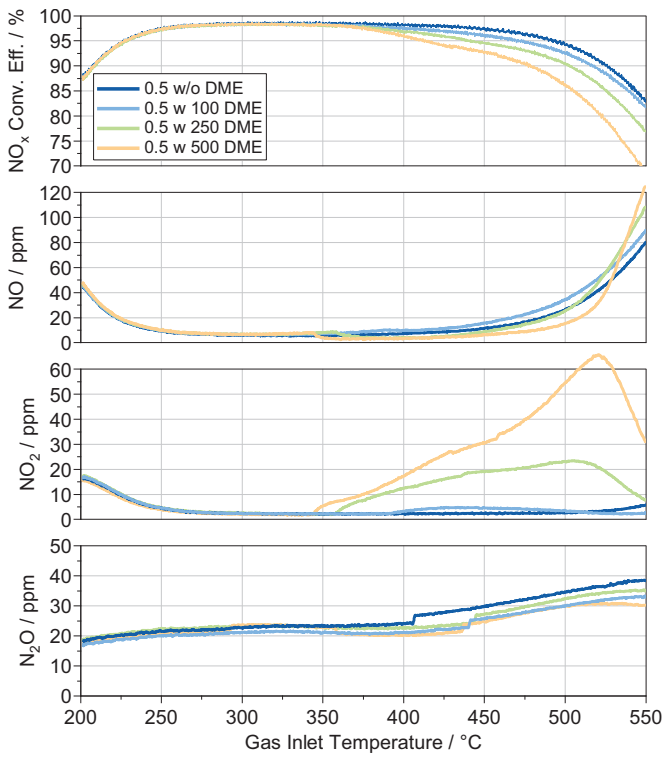

Fig. 15. NO_x conversion efficiency, NO concentration, NO_2 concentration and N_2O concentration over catalyst inlet temperature during NH_3-TPR of SCR 1 for fast SCR conditions in the case of $c_{DME} = 0$ ppm (blue), $c_{DME} = 100$ ppm (light blue), $c_{DME} = 250$ ppm (green) and $c_{DME} = 500$ ppm (orange).

4. Conclusions

Our study unveils significant insights into the behavior of dimethyl ether (DME) across a relevant range of diesel oxidation catalysts (DOCs) and selective catalytic reduction (SCR) catalysts, summarized in the following bullets.

- All DOCs contain both Pt and Pd, with varying Pt/Pd ratios for the respective coated zones.
- DOC 3 has been identified as developed for an increased HC and NO_x storage capacity due to its zeolite composition.
- For the SCR catalysts, the conclusion is made that the active material is copper exchanged zeolite.
- With regard to the catalytic activity, DME proves challenging to convert on all DOCs, potentially resulting in DME slip onto subsequent SCR systems. In comparison to the C_3H_6 emitted in standard diesel exhaust, the light-off temperature for the examined DOCs is shifted by at least $T_{50} > 100$ °C to higher temperatures.
- DME oxidation can lead to secondary emissions over all DOCs. Formaldehyde formation occurs via two distinct mechanisms dependent on gas composition.
- DME slip emissions from the DOC have a notable influence on all SCR catalysts. They cause a reduction in NO_x conversion efficiency and form secondary emissions at elevated temperatures.
- Through temperature-programmed desorption (TPD) analysis, it is observed that DME itself does not compete with NH_3 during adsorption.
- At elevated temperatures of $T > 350$ °C DME decomposes also to CH_2O. The formaldehyde then could react with NH_3, which is proposed to lead to an enlarged storage capacity. An assumed HMT formation and decomposition forms hazardous compounds like hydrogen cyanide (HCN).
- NH_3 temperature-programmed reduction experiments (TPR) with the SCR catalysts show no direct influence on NO_x conversion efficiency under the presence of DME. Correlated to the decomposition products at elevated temperatures of $T > 350$ °C, the NO_x conversion is reduced.
- The formed secondary emission species and decomposition products during NH_3-SCR under DME presence are CH_3OH, CH_2O, CH_2O_2, CO and HCN. They are formed at temperatures of $T > 330$ °C.

Our findings underscore the challenges associated to DME, as a fuel with high drop-in potential into close to series production ICEs with an exhaust gas aftertreatment system comprising of a DOC and SCR. High light-off temperatures during the oxidation on the DOCs and the formation of toxic secondary emissions during the $DeNO_x$-SCR, alongside its inhibition state the challenge at hand. If, for example, DME were to be used as a neat fuel, or - as targeted in the DMEplusX project - as a DME/diesel fuel blend, DME would be present in the raw exhaust gas as fuel slip. Consequently, given the documented elevated DME light-off temperatures, a greater quantity of DME would slip the DOC, culminating in higher cumulative HC emissions and the potential formation of secondary emissions on the downstream SCR catalyst. It is imperative to direct particular attention to the highly toxic CH_2O, which is already subject to limits under U.S. emissions regulations. It is crucial to ascertain whether these modified boundary conditions hinder compliance with the limits in the emissions regulations, when employing DME as a drop-in fuel blend, while keeping the standard components for exhaust aftertreatment. This must be verified through additional investigations on the engine or via simulation. The results obtained in this study can be utilized directly in map-based simulation approaches.

Funding

The current work was funded by the Federal Ministry for Economic Affairs and Climate Action (BMWK, Bundesministerium für Wirtschaft und Klimaschutz) under the project "*DMEplusX, DME-containing renewable fuels for use in the legacy fleet*" (FKZ: 19I20018D) and the Deutsche Forschungsgemeinschaft (DFG, German Research Foundation) under Germany's Excellence Strategy – Cluster of Excellence 2186 "*The Fuel Science Center*" – ID: 390919832.

CRediT authorship contribution statement

Tom Padeken: Writing – original draft, Investigation, Conceptualization. **Ariel Augusto Schönberger:** Writing – original draft, Investigation, Conceptualization. **Nedelina Toshkova:** Writing – original draft, Investigation. **Alexander Lampkowski:** Writing – original draft. **Peter Mauermann:** Methodology, Conceptualization. **Daniel Röhrens:** Writing – original draft, Investigation. **Felix Ott:** Writing – original draft, Investigation. **Bastian Lehrheuer:** Writing – review & editing, Supervision. **Stefan Sterlepper:** Writing – review & editing, Supervision. **Ulrich Simon:** Writing – review & editing, Supervision. **Regina Palkovits:** Writing – review & editing, Supervision. **Stefan Pischinger:** Writing – review & editing, Supervision.

Declaration of competing interest

The authors declare that they have no known competing financial interests or personal relationships that could have appeared to influence the work reported in this paper.

Acknowledgements

The authors would particularly like to thank all members of the DMEplusX project group for their helpful feedback. We also would like to thank Mr. Günter Ernst Wesch, Mr. Volker Reimann, Ms. Cora Bischoff, Mr. Daniel Guillermo Melián Esser and Ms. Nergiz Yilmaz for their

experimental support during the investigations on the synthetic gas test bench. Special thanks are also expressed to Ford Motor Company for providing catalyst components required for the investigations.

Appendix A. Supplementary data

Supplementary data to this article can be found online at https://doi.org/10.1016/j.cej.2026.178969.

Data availability

https://doi.org/10.5281/zenodo.17807380

References

[1] CC BY 4.0, IEA, Transport, Paris, 2022.
[2] D. Bongartz, L. Doré, K. Eichler, T. Grube, B. Heuser, L.E. Hombach, M. Robinius, S. Pischinger, D. Stolten, G. Walther, A. Mitsos, Comparison of light-duty transportation fuels produced from renewable hydrogen and green carbon dioxide, Appl. Energy 231 (2018) 757–767.
[3] M. Zubel, T. Ottenwälder, B. Heuser, S. Pischinger, Combustion system optimization for dimethyl ether using a genetic algorithm, Int. J. Engine Res. 22 (2021) 22–38.
[4] Y. Putrasari, O. Lim, Dimethyl ether as the next generation fuel to control nitrogen oxides and particulate matter emissions from internal combustion engines: a review, ACS Omega 7 (2022) 32–37.
[5] J. Sun, G. Yang, Y. Yoneyama, N. Tsubaki, Catalysis chemistry of dimethyl ether synthesis, ACS Catal. 4 (2014) 3346–3356.
[6] S. Banivaheb, S. Pitter, K.H. Delgado, M. Rubin, J. Sauer, R. Dittmeyer, Recent progress in direct DME synthesis and potential of bifunctional catalysts, Chem. Ing. Tech. 94 (2022) 240–255.
[7] C. Zhou, N. Wang, Y. Qian, X. Liu, J. Caro, A. Huang, Efficient synthesis of dimethyl ether from methanol in a bifunctional zeolite membrane reactor, Angew. Chem. Int. Ed. Eng. 55 (2016) 12678–12682.
[8] F. Pontzen, W. Liebner, V. Gronemann, M. Rothaemel, B. Ahlers, CO_2-based methanol and DME - efficient technologies for industrial scale production, Catal. Today 171 (2011) 242–250.
[9] E. Lam, J.J. Corral-Pérez, K. Larmier, G. Noh, P. Wolf, A. Comas-Vives, A. Urakawa, C. Copéret, CO_2 hydrogenation on Cu/Al_2O_3 role of the metal/support interface in driving activity and selectivity of a bifunctional catalyst, Angew. Chem. Int. Ed. 58 (2019) 13989–13996.
[10] S.H. Park, C.S. Lee, Applicability of dimethyl ether (DME) in a compression ignition engine as an alternative fuel, Energy Convers. Manag. 86 (2014) 848–863.
[11] W. Appel, H. Brähler, S. Breuer, U. Dahlhaus, T. Esch, E. Hoepke, S. Kopp, B. Rhein, Nutzfahrzeugtechnik, Vieweg+Teubner Verlag, Wiesbaden, 2013.
[12] B. Elvers, A. Schütze (Eds.), Handbook of Fuels, Wiley, 2021.
[13] C.K. Lambert, Current state of the art and future needs for automotive exhaust catalysis, Nat. Catal. 2 (2019) 554–557.
[14] S. Tamm, H.H. Ingelsten, M. Skoglundh, A.E. Palmqvist, Mechanistic aspects of the selective catalytic reduction of NO_x by dimethyl ether and methanol over γ-Al_2O_3, J. Catal. 276 (2010) 402–411.
[15] S. Sitshebo, A. Tsolakis, K. Theinnoi, Promoting hydrocarbon-SCR of NO_x in diesel engine exhaust by hydrogen and fuel reforming, Int. J. Hydrog. Energy 34 (2009) 7842–7850.
[16] B. Choi, K. Lee, G. Son, Review of recent after-treatment technologies for De-NO_x process in diesel engines, Int. J. Automot. Technol. 21 (2020) 1597–1618.
[17] J.A. Martens, A. Cauvel, A. Francis, C. Hermans, F. Jayat, M. Remy, M. Keung, J. Lievens, P.A. Jacobs, NOx abatement in exhaust from lean-burn combustion engines by reduction of NO_2 over silver-containing zeolite catalysts, Angew. Chem. Int. Ed. 37 (1998) 1901–1903.
[18] G. Shibata, K. Tanaka, Y. Chiba, H. Ogawa, M. Shimokawabe, EE1-1 NO_x reduction characteristics of DME-SCR system for diesel engines (EE: exhaust emissions and measurement, general session papers), in: The Proceedings of the International Symposium on Diagnostics and Modeling of Combustion in Internal Combustion Engines 2012.8, 2012, pp. 263–268.
[19] I. Nova, E. Tronconi, Urea-SCR Technology for deNOx After Treatment of Diesel Exhausts, Springer New York, New York, NY, 2014.
[20] D. Maizak, T. Wilberforce, A.G. Olabi, DeNOx removal techniques for automotive applications - a review, Environ. Adv. 2 (2020) 100021.
[21] G. Ertl, H. Knzinger, F. Schüth, J. Weitkamp, Handbook of Heterogeneous Catalysis, Wiley-VCH Verlag GmbH & Co. KGaA, Weinheim, Germany, 2008.
[22] P. Forzatti, I. Nova, E. Tronconi, Enhanced NH_3 selective catalytic reduction for NO_x abatement, Angew. Chem. Int. Ed. Eng. 48 (2009) 8366–8368.
[23] A. Ishikawa, M. Neurock, E. Iglesia, Structural requirements and reaction pathways in dimethyl ether combustion catalyzed by supported Pt clusters, J. Am. Chem. Soc. 129 (2007) 13201–13212.
[24] F. Solymosi, J. Cserényi, L. Ovári, A comparative study of the complete oxidation of dimethyl ether on supported group VIII metals, Catal. Lett. 44 (1997) 89–93.
[25] F. Martinovic, F.A. Deorsola, M. Armandi, B. Bonelli, R. Palkovits, S. Bensaid, R. Pirone, Composite Cu-SSZ-13 and CeO_2-SnO_2 for enhanced NH_3-SCR resistance towards hydrocarbon deactivation, Appl. Catal. B Environ. 282 (2021) 119536.
[26] I. Heo, S. Sung, M.B. Park, T.S. Chang, Y.J. Kim, B.K. Cho, S.B. Hong, J.W. Choung, I.-S. Nam, Effect of hydrocarbon on DeNOx performance of selective catalytic reduction by a combined reductant over cu-containing zeolite catalysts, ACS Catal. 9 (2019) 9800–9812.
[27] F. Gramigni, U. Iacobone, N.D. Nasello, T. Selleri, N. Usberti, I. Nova, Review of hydrocarbon poisoning and deactivation effects on cu-zeolite, Fe-zeolite, and vanadium-based selective catalytic reduction catalysts for NO_x removal from lean exhausts, Ind. Eng. Chem. Res. 60 (2021) 6403–6420.
[28] I. Malpartida, O. Marie, P. Bazin, M. Daturi, X. Jeandel, An operando IR study of the unburnt HC effect on the activity of a commercial automotive catalyst for NH_3-SCR, Appl. Catal. B Environ. 102 (2011) 190–200.
[29] D. Zengel, P. Koch, B. Torkashvand, J.-D. Grunwaldt, M. Casapu, O. Deutschmann, Emission of toxic HCN during NO_x removal by ammonia SCR in the exhaust of lean-burn natural gas engines, Angew. Chem. Int. Ed. 59 (2020) 14423–14428.
[30] D. Damma, P. Ettireddy, B. Reddy, P. Smirniotis, A review of low temperature NH_3-SCR for removal of NO_x, Catalysts 9 (2019) 349.
[31] N.R. Jaegers, J.-K. Lai, Y. He, E. Walter, D.A. Dixon, M. Vasiliu, Y. Chen, C. Wang, M.Y. Hu, K.T. Mueller, I.E. Wachs, Y. Wang, J.Z. Hu, Mechanism by which tungsten oxide promotes the activity of supported V_2O_5/TiO_2 catalysts for NO_X abatement: structural effects revealed by ^{51}V MAS NMR spectroscopy, Angew. Chem. Int. Ed. 58 (2019) 12609–12616.
[32] Y. Xin, Q. Li, Z. Zhang, Zeolitic materials for DeNO_x selective catalytic reduction, ChemCatChem 10 (2018) 29–41.
[33] T. Ryu, N.H. Ahn, S. Seo, J. Cho, H. Kim, D. Jo, G.T. Park, P.S. Kim, C.H. Kim, E. L. Bruce, P.A. Wright, I.-S. Nam, S.B. Hong, Fully copper-exchanged high-silica LTA zeolites as unrivaled hydrothermally stable NH_3-SCR catalysts, Angew. Chem. Int. Ed. 56 (2017) 3256–3260.
[34] X. Ye, J.E. Schmidt, R.-P. Wang, I.K. van Ravenhorst, R. Oord, T. Chen, F. de Groot, F. Meirer, B.M. Weckhuysen, Deactivation of Cu-exchanged automotive-emission NH_3-SCR catalysts elucidated with nanoscale resolution using scanning transmission X-ray microscopy, Angew. Chem. Int. Ed. 59 (2020) 15610–15617.
[35] T.V.W. Janssens, H. Falsig, L.F. Lundegaard, P.N.R. Vennestrøm, S.B. Rasmussen, P. G. Moses, F. Giordanino, E. Borfecchia, K.A. Lomachenko, C. Lamberti, S. Bordiga, A. Godiksen, S. Mossin, P. Beato, A consistent reaction scheme for the selective catalytic reduction of nitrogen oxides with ammonia, ACS Catal. 5 (2015) 2832–2845.
[36] W. Hu, T. Selleri, F. Gramigni, E. Fenes, K.R. Rout, S. Liu, I. Nova, Chen, X. Gao, E. Tronconi, On the redox mechanism of low-temperature NH3-SCR over Cu-CHA: a combined experimental and theoretical study of the reduction half cycle, Angew. Chem. Int. Ed. Eng. 60 (2021) 7197–7204.
[37] C. Paolucci, A.A. Verma, S.A. Bates, V.F. Kispersky, J.T. Miller, R. Gounder, W. N. Delgass, F.H. Ribeiro, W.F. Schneider, Isolation of the copper redox steps in the standard selective catalytic reduction on Cu-SSZ-13, Angew. Chem. Int. Ed. 53 (2014) 11828–11833.
[38] F. Gao, E.D. Walter, M. Kollar, Y. Wang, J. Szanyi, C.H. Peden, Understanding ammonia selective catalytic reduction kinetics over Cu/SSZ-13 from motion of the Cu ions, J. Catal. 319 (2014) 1–14.
[39] C. Paolucci, I. Khurana, A.A. Parekh, S. Li, A.J. Shih, H. Li, J.R. Di Iorio, J. D. Albarracin-Caballero, A. Yezerets, J.T. Miller, W.N. Delgass, F.H. Ribeiro, W. F. Schneider, R. Gounder, Dynamic multinuclear sites formed by mobilized copper ions in NO_x selective catalytic reduction, Science (New York, N.Y.) 357 (2017) 898–903.
[40] Y. Zhang, Y. Peng, K. Li, S. Liu, J. Chen, J. Li, F. Gao, C.H.F. Peden, Using transient FTIR spectroscopy to probe active sites and reaction intermediates for selective catalytic reduction of NO on Cu/SSZ-13 catalysts, ACS Catal. 9 (2019) 6137–6145.
[41] F. Gao, D. Mei, Y. Wang, J. Szanyi, C.H.F. Peden, Selective catalytic reduction over Cu/SSZ-13: linking homo- and heterogeneous catalysis, J. Am. Chem. Soc. 139 (2017) 4935–4942.
[42] Y. Zhang, J. Zhang, H. Wang, W. Yang, C. Wang, Y. Peng, J. Chen, J. Li, F. Gao, Selective catalytic reduction of NO_x with NH_3 over Cu/SSZ-13: elucidating dynamics of cu active sites with in situ UV-vis spectroscopy and DFT calculations, J. Phys. Chem. C 126 (2022) 8720–8733.
[43] P. Chen, A. Khetan, M. Jabłońska, J. Simböck, M. Muhler, R. Palkovits, H. Pitsch, U. Simon, Local dynamics of copper active sites in zeolite catalysts for selective catalytic reduction of NO_x with NH_3, Appl. Catal. B Environ. 237 (2018) 263–272.
[44] A.J. O'Malley, M. Sarwar, J. Armstrong, C.R.A. Catlow, I.P. Silverwood, A.P. E. York, I. Hitchcock, Comparing ammonia diffusion in NH_3-SCR zeolite catalysts: a quasielastic neutron scattering and molecular dynamics simulation study, Phys. Chem. Chem. Phys. 20 (2018) 11976–11986.
[45] W. Hu, F. Gramigni, N.D. Nasello, N. Usberti, U. Iacobone, S. Liu, I. Nova, X. Gao, E. Tronconi, Dynamic binuclear Cu II sites in the reduction half-cycle of low-temperature NH_3-SCR over Cu-CHA catalysts, ACS Catal. 12 (2022) 5263–5274.
[46] L. Chen, H. Falsig, T.V. Janssens, H. Grönbeck, Activation of oxygen on (NH_3Cu NH_3)+ in NH_3-SCR over Cu-CHA, J. Catal. 358 (2018) 179–186.
[47] M. Jabłońska, A. Mollá Robles, M. Rotko, T.H. Vuong, H. Lei, Ž. Lavrič, M. Grilc, M. F. Lukman, R. Valiullin, M. Bertmer, J. Möllmer, J. Rabeah, A. Pöppl, U. Simon, R. Gläser, Unraveling the NH_3-SCR-DeNO_x mechanism of Cu-SSZ-13 variants by spectroscopic and transient techniques, ChemSusChem 17 (2024) e202400198.
[48] Y. Fu, W. Ding, H. Lei, Y. Sun, J. Du, Y. Yu, U. Simon, P. Chen, Y. Shan, G. He, H. He, Spatial distribution of Brønsted acid sites determines the mobility of reactive Cu ions in the Cu-SSZ-13 catalyst during the selective catalytic reduction of NO_x with NH_3, J. Am. Chem. Soc. 146 (2024) 11141–11151.
[49] F. Gao, J. Szanyi, On the hydrothermal stability of Cu/SSZ-13 SCR catalysts, Appl. Catal. A Gen. 560 (2018) 185–194.
[50] A.A. Schönberger, G.M. Haselmann, B. Wolkenar, S. Schönebaum, P. Mauermann, S. Sterlepper, S. Pischinger, U. Simon, Sorption and reaction of biomass derived HC

blends and their constituents on a commercial Pt–Pd/Al_2O_3 oxidation catalyst, Catal. Lett. 152 (2022) 1880–1894.
[51] B. Wolkenar, S. Schönebaum, P. Mauermann, P. Dittmann, S. Pischinger, U. Simon, Storage and oxidation of oxygen-free and oxygenated hydrocarbons on a Pt–Pd series production oxidation catalyst, Top. Catal. 62 (2019) 376–385.
[52] C. Özyalcin, P. Mauermann, J. Dornseiffer, S. Sterlepper, M. Günther, S. Pischinger, Contributions of washcoat components in different configurations to the NO_X and oxygen storage performance of LNT catalysts, Catalysts 12 (2022) 953.
[53] T. Padeken, A. Lampkowski, P. Mauermann, W. Willems, C. Nederlof, B. Franzke, S. Sterlepper, B. Lehrheuer, S. Pischinger, Dataset for DME oxidation behavior of commercial Pt/Pd-series diesel oxidation catalysts, Data Brief 64 (2026) 112380.
[54] A.A. Schönberger Alvarez, C. Özyalcin, T. Padeken, P. Mauermann, B. Lehrheuer, S. Sterlepper, A. Abouserie, M. Vennewald, U. Simon, R. Palkovits, S. Pischinger, Impact of unintentionally formed CH_2O in oxygenated fuel exhausts on DeNO$_x$-SCR at different NO_2/NO_x ratios under close to real conditions, Catal. Sci. Technol. 13 (2023) 4069–4081.
[55] X. Auvray, L. Olsson, Stability and activity of Pd-, Pt- and Pd–Pt catalysts supported on alumina for NO oxidation, Appl. Catal. B Environ. 168–169 (2015) 342–352.
[56] A.F.W. Chiffey, P.R.R. Phillips, F. Moreau, C.R. Daly, M. O'Brien, WO 2015/150805 (08.10.2015 Gazette 2015/40), 2015.
[57] F. Gao, N.M. Washton, Y. Wang, M. Kollár, J. Szanyi, C.H. Peden, Effects of Si/Al ratio on Cu/SSZ-13 NH_3-SCR catalysts: implications for the active Cu species and the roles of Brønsted acidity, J. Catal. 331 (2015) 25–38.
[58] A.A. Schönberger Alvarez, I.C. Özyalcin, T. Padeken, P. Mauermann, B. Lehrheuer, S. Sterlepper, A. Abouserie, M. Vennewald, U. Simon, R. Palkovits, S. Pischinger, Dataset for the Publication: Impact of Unintentionally Formed CH_2O in Oxygenated Fuel Exhausts on DeNOx-SCR at Different NO_2/NO_x Ratios Under Close to Real Conditions, Zenodo, 2024.
[59] K. Hauff, U. Tuttlies, G. Eigenberger, U. Nieken, A global description of DOC kinetics for catalysts with different platinum loadings and aging status, Appl. Catal. B Environ. 100 (2010) 10–18.
[60] L. Glover, R. Douglas, G. McCullough, M. Keenan, P. Revereault, C. McAtee (Eds.), Performance Characterisation of a Range of Diesel Oxidation Catalysts: Effect of Pt: Pd Ratio on Light Off Behaviour and Nitrogen Species Formation, SAE International400 Commonwealth Drive, Warrendale, PA, United States, 2011.
[61] A. Ishikawa, E. Iglesia, Bifunctional pathways mediated by Pt clusters and Al_2O_3 in the catalytic combustion of dimethyl ether, Chem. Commun. (Camb.) (2007) 2992–2993.
[62] R. Peláez, P. Marín, S. Ordóñez, Synthesis of formaldehyde from dimethyl ether on alumina-supported molybdenum oxide catalyst, Appl. Catal. A Gen. 527 (2016) 137–145.
[63] P. Cheung, Liu, E. Iglesia, Kinetics and mechanism of dimethyl ether oxidation to formaldehyde on supported molybdenum oxide domains, J. Phys. Chem. B 108 (2004) 18650–18658.
[64] H. Liu, P. Cheung, E. Iglesia, Zirconia-supported MoO_x catalysts for the selective oxidation of dimethyl ether to formaldehyde: structure, redox properties, and reaction pathways, J. Phys. Chem. B 107 (2003) 4118–4127.
[65] X. Huang, Y. Li, Y. Xu, W. Shen, Kinetics of selective oxidation of dimethyl ether to formaldehyde over Al_2O_3-supported VO_x and MoO_x catalysts, Catal. Lett. 97 (2004) 185–190.
[66] L. Bugyi, F. Solymosi, Adsorption and dissociation of dimethyl ether on clean and oxygen-dosed Rh(111), Surf. Sci. 385 (1997) 365–375.
[67] J.G. Chen, P. Basu, T.H. Ballinger, J.T. Yates, A transmission infrared spectroscopic investigation of the reaction of dimethyl ether with alumina surfaces, Langmuir 5 (1989) 352–356.
[68] C. Lambert, D. Dobson, C. Gierczak, G. Guo, J. Ura, J. Warner, Nitrous oxide emissions from a medium-duty diesel truck exhaust system, Int. J. Powertrains 3 (1) (2014) 4–25, https://doi.org/10.1504/IJPT.2014.059410.
[69] Z. Hong, Z. Wang, X. Li, Catalytic oxidation of nitric oxide (NO) over different catalysts: an overview, Catal. Sci. Technol. 7 (2017) 3440–3452.
[70] R. Burch, P.J. Millington, A.P. Walker, Mechanism of the selective reduction of nitrogen monoxide on platinum-based catalysts in the presence of excess oxygen, Appl. Catal. B Environ. 4 (1994) 65–94.
[71] P. Lott, S. Bastian, H. Többen, L. Zimmermann, O. Deutschmann, Formation of nitrous oxide over Pt-Pd oxidation catalysts: secondary emissions by interaction of hydrocarbons and nitric oxide, Appl. Catal. A Gen. 651 (2023) 119028.
[72] J. Li, R. Zhu, Y. Cheng, C.K. Lambert, R.T. Yang, Mechanism of propene poisoning on Fe-ZSM-5 for selective catalytic reduction of NO(x) with ammonia, Environ. Sci. Technol. 44 (2010) 1799–1805.
[73] J.-Y. Luo, H. Oh, C. Henry, W. Epling, Effect of C_3H_6 on selective catalytic reduction of NO_x by NH_3 over a Cu/zeolite catalyst: a mechanistic study, Appl. Catal. B Environ. 123–124 (2012) 296–305.
[74] H. Zhao, X. Wu, Z. Huang, H. Shen, J. Dong, X. Li, G. Jing, Changes of the C_3H_6-poisoning effect over a Cu-SSZ-13 NH_3-SCR catalyst upon hydrothermal treatment at different temperatures, Energy Fuel 36 (2022) 2712–2721.
[75] I. Heo, Y. Lee, I.-S. Nam, J.W. Choung, J.-H. Lee, H.-J. Kim, Effect of hydrocarbon slip on NO removal activity of $CuZSM_5$, $FeZSM_5$ and V_2O_5/TiO_2 catalysts by NH_3, Microporous Mesoporous Mater. 141 (2011) 8–15.
[76] M.U. Alzueta, J. Muro, R. Bilbao, P. Glarborg, Oxidation of dimethyl ether and its interaction with nitrogen oxides, Isr. J. Chem. 39 (1999) 73–86.
[77] T. Yamamoto, S. Kajimura, Kinetic study on NO reduction using dimethyl ether as a reburning fuel, Energy Fuel 31 (2017) 12500–12507.
[78] I.O. Liu, N.W. Cant, M. Kögel, T. Turek, The formation of HCN during the reduction of NO by isobutane over Fe-MFI made by solid-state ion exchange, Catal. Lett. 63 (1999) 241–244.
[79] M. Chun-lan, Z. Yu-sheng, S. Yu, H. Jian, S. Hai-ying, Experimental and numerical study on emission in an HCCI engine operated with neat dimethyl ether, in: SAE Technical Paper Series, SAE International400 Commonwealth Drive, Warrendale, PA, United States, 2007.
[80] S. Tamm, H.H. Ingelsten, A.E.C. Palmqvist, Influence of gas phase reactions on DME-SCR over γ-alumina, Catal. Lett. 141 (2011) 656–664.
[81] S. Tamm, H.H. Ingelsten, M. Skoglundh, A.E. Palmqvist, The influence of gas phase reactions on the design criteria for catalysts for lean NO_x reduction with dimethyl ether, Appl. Catal. B Environ. 91 (2009) 234–241.
[82] S. Su, P. Zaza, A. Renken, Catalytic dehydrogenation of methanol to water-free formaldehyde, Chem. Eng. Technol. 17 (1994) 34–40.